Energy & Environmental Science

ROYAL SOCIETY OF CHEMISTRY

PAPER

View Article Online
View Journal | View Issue

Cite this: *Energy Environ. Sci.*, 2024, **17**, 5730

Uncovering fast solid-acid proton conductors based on dynamics of polyanion groups and proton bonding strength†

Pjotrs Žguns, ‡[a] Konstantin Klyukin, ‡[ac] Louis S. Wang, [d] Grace Xiong, [d] Ju Li, [ab] Sossina M. Haile [d] and Bilge Yildiz *[ab]

Achieving high proton conductivity in inorganic solids is key for advancing many electrochemical technologies, including low-energy nano-electronics and energy-efficient fuel cells and electrolyzers. A quantitative understanding of the physical traits of a material that regulate proton diffusion is necessary for accelerating the discovery of fast proton conductors. In this work, we have mapped the structural, chemical and dynamic properties of solid acids to the elementary steps of the Grotthuss mechanism of proton diffusion. Our approach combines *ab initio* molecular dynamics simulations, analysis of phonon spectra and atomic structure calculations. We have identified the donor–hydrogen bond lengths and the acidity of polyanion groups as key descriptors of local proton transfer and the vibrational frequencies of the cation framework as the key descriptor of lattice flexibility. The latter facilitates rotations of polyanion groups and long-range proton migration in solid acid proton conductors. The calculated lattice flexibility also correlates with the experimentally reported superprotonic transition temperatures. Using these descriptors, we have screened the Materials Project database and identified potential solid acid proton conductors with monovalent, divalent and trivalent cations, including Ag^{+}, Sr^{2+}, Ba^{2+} and Er^{3+} cations, which go beyond the traditionally considered monovalent alkali cations (Cs^{+}, Rb^{+}, K^{+}, and NH_4^{+}) in solid acids.

Received 18th March 2024,
Accepted 18th June 2024

DOI: 10.1039/d4ee01219d

rsc.li/ees

Broader context

Discovery of fast proton conductors can significantly advance a wide range of technologies, including hydrogen fuel cells, electrolyzers, electrosynthesis of fuels, batteries and brain-inspired computing devices. Here, we identify promising fast proton conductors, focusing particularly on the class of solid acids, and go well beyond the traditionally considered chemistries. The key to this is having found physically based descriptors that map the structure and dynamics of the lattice to the atomistic mechanism of proton transport in solids, by leveraging computational tools, physical models, and extensive materials databases. These physical descriptors of proton conduction also provide paths for increasing the conductivity and decreasing the temperature of superprotonic transition. With the rapid growth of materials databases, our approach lays ground for the physically informed search of fast proton conductors and enlarges the chemical space of materials to power the green revolution.

Introduction

Inorganic solid electrolyte materials with high proton conductivity are important for advancing electrochemical devices for energy conversion, energy storage and energy-efficient computing, such as ceramic fuel cells and electrolyzers,[1–5] solid acid fuel cells,[6–8] hydrogen generators,[9] solid-state proton batteries,[10,11] electrochromic devices,[12] and magneto-ionic[13,14] and analog neuromorphic[15–18] computing hardware. Although high proton conductivities are reported for a range of material classes,[19–22] most of them show slow proton conductivity at low temperatures (*i.e.*, at room temperature), require special conditions such as a humid environment, or are not compatible with

[a] *Department of Materials Science and Engineering, Massachusetts Institute of Technology, 77 Massachusetts Avenue, Cambridge, Massachusetts 02139, USA. E-mail: byildiz@mit.edu*
[b] *Department of Nuclear Science and Engineering, Massachusetts Institute of Technology, 77 Massachusetts Avenue, Cambridge, Massachusetts 02139, USA*
[c] *Department of Materials Engineering, Auburn University, Auburn, Alabama 36849, USA*
[d] *Department of Materials Science and Engineering, Northwestern University, Evanston, IL 60208, USA*

† Electronic supplementary information (ESI) available. See DOI: https://doi.org/10.1039/d4ee01219d

‡ These authors contributed equally to this work.

particular technological standards. For example, state-of-the-art perovskite oxide ceramic electrolytes demonstrate sizable proton conductivity (10^{-3} S cm^{-1}) only above ~300 °C.[22] At lower temperatures, proton diffusion in the bulk of perovskites is slow, and the reported room temperature conductivities are attributed to accumulated water interlayers, *e.g.*, along grain boundaries or nanopores, rather than diffusion in the bulk lattice.[22] Metal–organic frameworks (MOFs)[23] and polymers such as Nafion[24] provide a conductivity of up to 10^{-2} S cm^{-1} at room temperature. These materials often require high humidity to conduct protons, and they are typically permeable to alcohols rendering them inapplicable for power generation using such fuels. Furthermore, they are incompatible with the processing of nanoelectronics using the complementary metal-oxide semiconductor (CMOS) technology. Novel solid-state proton conductors are sought after for near ambient-temperature applications. A quantitative understanding of the critical physical, structural, and chemical traits of a material that control proton conduction is necessary for developing the respective materials design strategies.

Solid acids constitute a promising class of proton conductors.[19,25] Solid acids are composed of metal cations and a network of polyanion groups (*e.g.*, SeO_4, SO_4, and PO_4) that normally do not share corners or edges and are linked solely by hydrogen bonds. At low temperatures, the rigid hydrogen bonding network in solid acids results in low proton conductivities (~10^{-5} S cm^{-1}).[6,19] In the solid acids that exhibit high conductivities (>10^{-3} S cm^{-1}), fast proton transport is achieved above the T_{sp} temperature of first-order, superprotonic transition (T_{sp} is typically within 100–300 °C).[6,19,25] The characteristic features of the superprotonic phase are facile rotation of polyanion groups (which even leads to their rotational disorder) and the accompanying dynamical disorder of hydrogen bond networks.[19,25] Both of these traits enable fast proton conduction *via* the Grotthuss mechanism[19,26] above the T_{sp} in solid acids. The rich compositional space available for solid acids allows tuning the properties of these compounds and potentially achieving high proton conductivity at lower temperatures.

High-throughput computational screening of materials is a promising approach for identifying fast proton conductors. Recently, extensive efforts have been devoted to screening solid-state Li-ions[27–34] and O-conductors,[34–36] allowing one to identify and experimentally verify promising solid-state electrolytes for the advancement of solid-state batteries and fuel cell technologies. The undertaken screening approaches can be broadly classified into three groups that use: (1) interpretable physical descriptors that are based on the ion diffusion mechanism,[29,33] (2) a data-driven approach to train machine learning models but not necessarily provide interpretable insights into the microscopic origin of why certain compounds are better ionic conductors than others,[27,30,35–37] and (3) high-throughput molecular dynamics (MD) simulations[28] to directly probe ionic diffusivities of screened compounds. Among the first two approaches, the first one that incorporates physical laws governing the microscopic diffusion mechanism into the screening makes models more robust and interpretable and thus may be deemed superior[38] to the second one.

Computational screening for better proton conductors has been mostly limited to perovskites and related oxides.[36,39–41] It was found that the energy barriers for the covalent O–H bond rotation and proton transfer between acceptors and donors correlate with the energy of the O–H bond.[42] High-throughput studies of double-perovskites[40] and ternary oxides[41] revealed a correlation of the proton transfer barrier with the proton–acceptor distance, $d_{H\cdots O}$, as well as with the B-cation radius.[40] Another study demonstrated that oxygen affinity in the vicinity of dopants correlates positively with experimentally measured proton conductivities.[43] Recently developed machine learning models used experimental data to link extrinsic parameters such as temperature and chemical composition to proton concentrations in perovskite oxides,[36,39] without providing microscopic insights into the meaning of these extrinsic parameters. To the best of our knowledge, a search for physical descriptors and high throughput screening of proton-conducting electrolytes other than perovskites and related ceramic oxides have not been previously reported.

In this work, we consider materials that have hydrogen in their chemical formula and particularly examine the class of solid acids. We impose this limitation (that H is part of the structure) to focus on proton migration and its rate-limiting factors, without the need to consider the thermodynamics of proton incorporation. We first identify the physical descriptors of fast proton conduction in solid acids by establishing correlations between candidate descriptors and proton conductivities computed by means of *ab initio* molecular dynamics (AIMD) simulations. Next, we screen compounds from the Materials Project[44] database (that were also reported as existing under ambient conditions according to the ICSD[45] database) to select promising materials and then calculate their proton conductivity using machine-learning accelerated AIMD.[46–48] A detailed description of computational methods is available in Section S1 (ESI†). Through these methods we identify promising solid acid proton conductors containing cations outside of the traditionally considered monovalent alkali cation-based solid acids (Cs^+, Rb^+, K^+, and NH_4^+). These include the monovalent cations Ag^+ and Tl^+ as well as the divalent and trivalent cations such as Ba^{2+}, Sr^{2+} and Er^{3+}. In addition, we show that the descriptors of high proton conductivity, in particular lattice flexibility, may also be useful for predicting the transition temperature in known superprotonic conductors. Our work demonstrates that understanding the physical descriptors of the governing proton conduction mechanism can allow identification of new material candidates with rationally targeted properties.

Descriptors of the Grotthuss mechanism

The Grotthuss mechanism[19,25,26] is the underlying proton conduction mechanism in solid acids. It is broadly a two-step process (Fig. 1) involving: (i) proton transfer from donor to

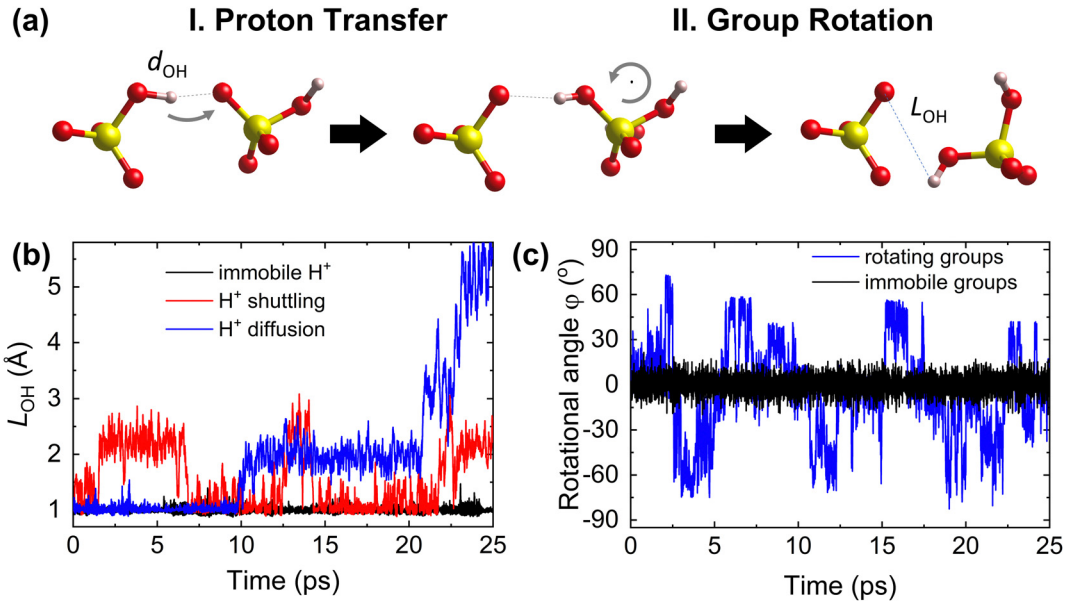

Fig. 1 Steps of proton diffusion *via* the Grotthuss mechanism in a solid acid. (a) Donor and acceptor groups in a solid acid (yellow: S, red: O, and pink: H) Left: the proton is covalently bound to the initial donor (O on the left) and forms a hydrogen bond with the initial acceptor (O on the right). Middle: the proton has hopped and is covalently bound to the initial acceptor. Right: the acceptor group has rotated, taking the proton further away from the initial donor. (b) Time evolution of the proton–donor distance, L_{OH}, calculated from AIMD trajectories, showing three cases of proton transfer kinetics: an immobile proton, proton "shuttling" (confinement to back-and-forth motion between the same donor and acceptor), and long-range proton diffusion. (c) Time evolution of the azimuthal angle, φ, characterizing group rotation, where φ is defined within the internal coordinate system for each group vector (see Section S1 in the ESI†), calculated from AIMD simulations, showing two cases: rotationally immobile groups ($\varphi \approx 0^{\circ}$) and rotationally mobile groups (displaying a large change of φ).

acceptor sites in which a covalent proton–donor bond is broken and a new covalent proton–acceptor bond is created and (ii) reorganization of the environment, specifically rotation of polyanion groups,[19,25,49] bringing the proton close to a new acceptor site and preventing a backward transfer to the original donor site.[19] For fast diffusion, the rates of both steps must be high. For example, slow or constrained rotation would confine protons to hopping mostly between the original donor and acceptor sites (Fig. 1). Below, we hypothesize descriptors of each step of the Grotthuss mechanism.

Proton transfer descriptors

Proton bonding to donor (D) and acceptor (A) atoms shows universal features. When the covalent D–H bond, d_{DH}, elongates, the hydrogen bond H···A, $d_{H\cdots A}$, shrinks, and *vice versa*.[50] Moreover, the inverse relation between d_{DH} and $d_{H\cdots A}$ is universal and holds well in various compounds.[19,50] This implies that the bond lengths d_{DH}, $d_{H\cdots A}$ and d_{DA} are interdependent,[51] such that any one of them can be used as a descriptor of hydrogen bonding strength or proton transfer ease. The energy barrier for proton transfer grows with increasing transfer distance between acceptor and donor sites.[19] In molecular complexes, the proton transfer is nearly barrierless for $d_{OO} \approx 2.4$ Å and the barrier increases to about 1 eV for $d_{OO} \approx 3$ Å.[19,52] Similar relations of the proton transfer barrier to the donor–acceptor distances, d_{DA}, were shown for perovskite oxides,[53,54] solid acids[49] and ternary oxides.[41] We expect that the proton barrier dependence on the bond lengths is general for different compounds with O–H···O bonds. Thus, we have assessed the covalent bond length, d_{DH}, as a descriptor of proton transfer in solid acids.

The energy barrier of proton transfer should similarly correlate with any other trait that reflects the D–H bond strength. For example, the acid dissociation constant, pK_a,[55–58] a common concept in liquid aqueous systems, reflects the extent of proton dissociation according to reaction: $H_3PO_4 + H_2O \rightarrow (H_2PO_4)^- + H_3O^+$, and we have assessed its relation to proton transfer in solid acids. Other possible descriptors include the bond stretching frequency[50] and bond order[50] or metrics that quantify the covalency of the donor–proton bond. The O 2p band center characterizes the covalence of bonds involving oxygen in metal oxides and is shown to correlate with the oxygen ion migration barrier[59] and hydrogen binding strength.[60] The position of O 2p states on the absolute energy scale was also found to correlate with proton affinity in closed-shell oxides.[61]

Group rotation descriptors

Rotational and network flexibilities are needed to enable the facile rotation of polyanion groups[19,25,49] to take the protons away from the vicinity of the original donor site. Superprotonic phase transition in solid acids is characterized by facile group rotations. This flexibility can be assessed from the lattice dynamics descriptors that reflect the rotational energy barrier. These include phonon band centers or phonon modes with a strong rotational character such as the so-called rigid unit modes.[62] Indeed, if rotational phonon modes of polyanion groups have a low frequency, one may expect[63] that the energy

barrier to group rotation is small. However, the identification of rotational modes of polyanion groups in solid acids and particularly their contribution to the Grotthuss mechanism is not trivial, as many modes may contribute to a rotational event. For high-throughput screening, we sought to describe the ease of rotation with a simple descriptor representing the most relevant modes. Along these lines, the force constants corresponding to octahedral rotations of low-frequency phonon modes were shown to correlate with oxygen anion interstitial migration barrier in Ruddlesden–Popper oxides.[64] Similarly, the average phonon band center of mobile Li-ion sites was found to correlate positively with their migration enthalpy.[63] The importance of the local structure[65] and lattice dynamics for proton[66] and hydrogen[67] conductivities was recently noted, and quantification of their role in proton conduction is desirable. For this purpose, as explained later, we have assessed the vibrational phonon modes of the framework cations as a proxy to the rotational flexibility of the polyanion groups.

Descriptors of group rotations may also be deduced from the topology of the hydrogen bonds or bonding constraints that rotating groups are subject to. For example, Maxwell has shown that frames (*e.g.*, made of struts and pins) are flexible if the number of degrees of freedom is larger than the number of constraints.[62,68] For solid acids, such analysis may include consideration of the number of bonds between the rotating groups and the rest of the crystal framework (*i.e.*, Cs–O in $CsHSO_4$). Although in solid acids the number of bonds can be very high (yet these ''bonds'' may be weak), they still develop exceptional rotational flexibility. Similarly, one may have to consider the topology of the hydrogen bonding network as it influences the rotations of polyanion groups.[19,25]

Summary of candidate descriptors

The complete set of hypothesized descriptors is summarized in Table 1. For proton transfer, we explicitly and quantitatively consider hydrogen bond lengths (both the covalent d_{OH} and the hydrogen bond $d_{H\cdots O}$), the acid dissociation constant, pK_a, and the O 2p band center position. The O–H stretching frequency was not assessed due to a higher computational cost as compared to d_{OH}. We did not find a generalizable correlation of the O 2p band center to the proton transport in our dataset (see Fig. S2 in the ESI†). While this could be due to various reasons, the relevant conclusion here is that the O 2p band center does not serve as a useful predictor of proton conductivity in solid acid materials. For rotational flexibility of the polyanion groups, we focused on the phonon modes of cations as a proxy, since the explicit assessment of the polyanion rotational modes and topological features was too complex to quantify across different structures and data sets.

Results and discussion

Descriptors of proton transfer

To test the proposed proton transfer descriptors (Table 1), we evaluated their correlation to the local metric of proton transfer, $L_{OH,max}$ (Fig. 1a and b) and the proton diffusivity, D_H, both extracted from AIMD simulations of 25 ps length at 700 K (see Section S1 in the ESI† for the comprehensive description of methods). $L_{OH} \approx 1.5$ Å is a typical mid-point between a donor and an acceptor. Thus, if $L_{OH,max} \lesssim 1.5$ Å, it can be concluded that the protons are immobile. Conversely, if $1.5 \text{ Å} \lesssim L_{OH,max} \lesssim 2$ Å, then proton transfer across the hydrogen bond occurred and if $L_{OH,max} \gtrsim 2$ Å, then the proton underwent additional diffusion (likely *via* polyanion group reorientation). Selecting $L_{OH,max} \approx 1.5$ Å defines a threshold metric for proton transfer, where larger values include both local proton transfer events and long-range proton diffusion.

Table 1 Hypothesized structural, chemical, and dynamic descriptors of the two steps of the Grotthuss mechanism of proton diffusion in inorganic solids in which the donor/acceptor is oxygen, O. The descriptors that were explored quantitatively in this work are marked with*

Descriptor	Property
Proton transfer	
d_{OH} (O–H bond length) (structural)*	O–H bond strength
$d_{H\cdots O}$ (H···O distance) (structural)*	H-bonding network
pK_a (acid dissociation constant) (chemical)*	Dissociation ease
ω_{OH} (O–H stretching frequency) (dynamic)	O–H bond strength
O 2p band center (electronic)*	O–H bond strength
Rotational flexibility	
Phonon modes of polyanion groups (dynamic)	Lattice flexibility
Phonon modes of cations (dynamic)*	Lattice flexibility
Topological features, constraints (structural)	Structural reorganization

The d_{OH} descriptor (defined as the largest of the O–H bond lengths in the initial structure; see Fig. 2a) showed a significant correlation with both $L_{OH,max}$ and D_H (Fig. 2b and c). All materials with a d_{OH} of > 1.007 Å demonstrated some proton transfer/diffusion, whereas materials with shorter O–H bonds demonstrated negligible transfer/diffusion. The ΔpK_a descriptor (the minimum absolute difference between the proton donor and acceptor group acidities) also showed a significant effect on both $L_{OH,max}$ and D_H (Fig. 2d and e). Nearly all materials with a ΔpK_a of < 5 demonstrated proton transfer/diffusion, whereas materials with larger ΔpK_a demonstrated negligible transfer/diffusion. Indeed, a large ΔpK_a value indicates that the energy difference between the acceptor and donor sites is large, which can increase the energy barrier.[69,70] The inherently low differences between the first and second and the second and third dissociation constants in sulfuric, phosphoric, arsenic, and selenic acids [58] are in agreement with fast local transport in superprotonic CsH_2PO_4,[71] CsH_2AsO_4,[71] $CsHSO_4$[72] and $CsHSeO_4$[72] and essentially indicate that the number of protons per polyanion group varies without incurring a high energy penalty, in support of the long-range proton transport. Among the two correlated descriptors (d_{OH} and ΔpK_a, see Fig. S3 in the ESI†), we expect that d_{OH} is more robust and accurate, encoding any structural/bonding variations in the solid that the tabulated pK_a values may not reflect. Therefore, we used d_{OH} in the final screening.

The data further show that the suggested criterion ($d_{OH} > 1.007$ Å) is necessary, but not sufficient, to identify fast

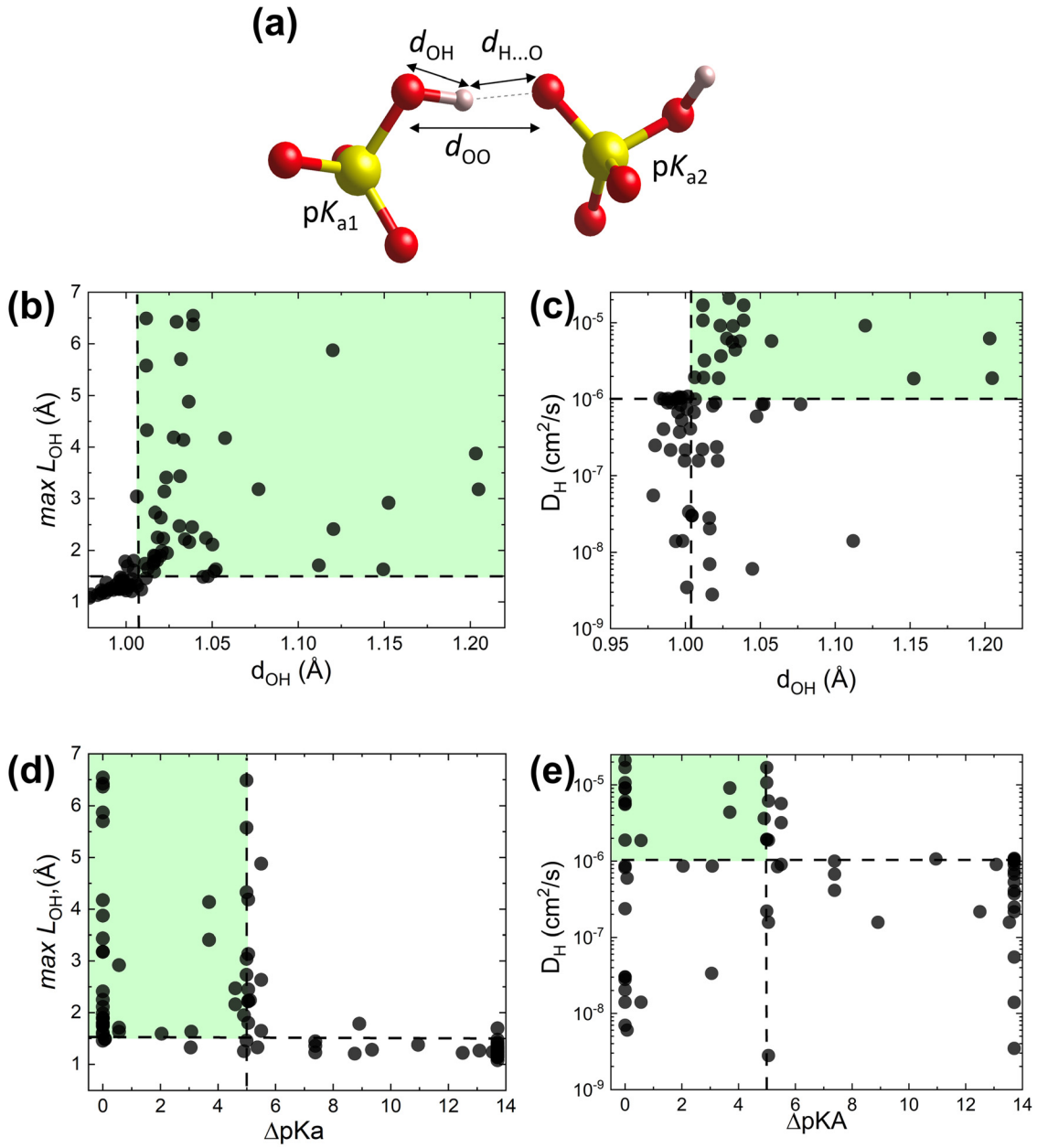

Fig. 2 AIMD results from the initial dataset to extract proton transfer descriptors. (a) Schematic showing d_{OH}, $d_{H\cdots O}$, d_{OO} and pK_a for donor and acceptor groups in a solid acid (color code: S is yellow, O is red, and H is pink). (b) Maximal distance travelled by the proton from its initial donor atom during the AIMD run, $L_{OH,max}$, *vs.* the maximal initial O–H bond length, d_{OH}. (c) Proton diffusivity, D_H *vs.* d_{OH}. (d) $L_{OH,max}$ *vs.* ΔpK_a. (e) D_H *vs.* ΔpK_a. All data at 700 K (the trajectory length is 25 ps). Dashed lines correspond to the selected cut-offs: D_H cut-off is set to 10^{-6} cm^2 s^{-1}, which corresponds to about 0.02 S cm^{-1} conductivity at 700 K and is above the AIMD accuracy limits (for further details see Computational methods, Section S1 in the ESI†).

conductors. Several examples of large d_{OH} materials show moderate values of $L_{OH,max}$ (~2 Å), Fig. 2b, and accordingly low diffusivities ($D_H < 10^{-6}$ cm^2 s^{-1}), Fig. 2c. Thus, by applying this criterion, we can filter out materials with a slow transfer rate (*viz.*, poor conductors), but not every remaining material will be a fast proton conductor.

Descriptors of group rotation

As indicated in Table 1, we have hypothesized cation phonon modes to control the ease of rotational motion of polyanion groups. Accordingly, we analyzed the vibrational modes associated with group rotation and the flexibility of the lattice. We found that rotational modes of polyanion groups are often accompanied by pronounced displacements of the framework cations. This observation is consistent with arguments from the literature.[19] Fig. 3a shows the pattern of atomic displacements for a selected low-frequency phonon mode in $CsHSO_4$. Cs cations execute pronounced excursions during the SO_4 group rotation. The framework created by the cesium cations must be flexible to enable frequent and extensive rotations of polyanion

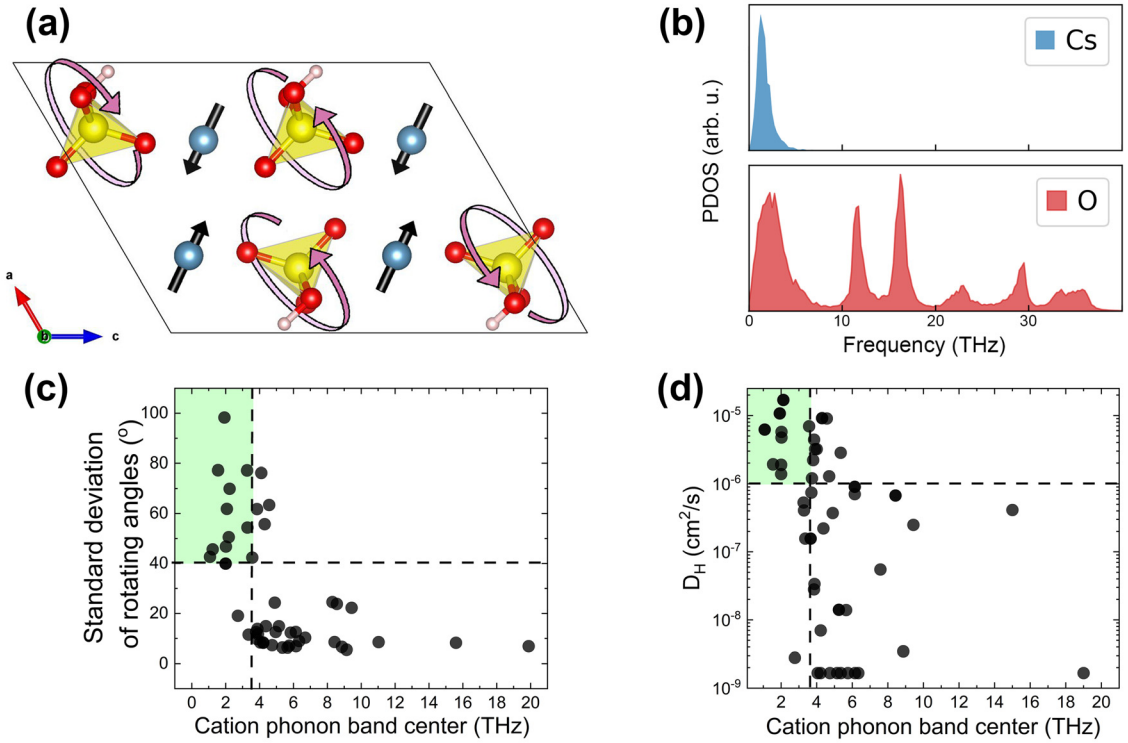

Fig. 3 AIMD results from the initial dataset to extract group rotation descriptors. (a) Schematic of a low-frequency mode of SO_4 rotations accompanied by large displacements of Cs cations in $CsHSO_4$ (mp-1192419, $P2_1/c$;[73] Cs is blue, S is yellow, O is red, and H is pink). The SO_4 unit is largely intact, *i.e.*, the S–O bonds are not stretched during this rotation. (b) Cation and oxygen phonon density of states of $CsHSO_4$ (estimated as the power spectrum of the atomic velocities). (c) Rotational metric (the larger of the standard deviations of the polar and azimuthal angles, θ and φ, in spherical coordinates, characterizing group rotation, see Section S1 in the ESI†) *vs.* the cation phonon band center. (d) Proton diffusivity, D_H, *vs.* the cation phonon band center. Compounds that do not possess mono-oxyanion groups were excluded from analysis (Table S1, ESI†). All data at 700 K.

tetrahedra. Remarkably, the cesium phonon spectrum in $CsHSO_4$ has a peak only in the low-frequency range, as seen in Fig. 3b. This is because the cesium ions do not form strong covalent bonds and are largely "detached" from the stretching and bending modes of SO_4 polyanions. This means that the cation phonon band center (ω_{cat}) can serve as a proxy for all the low-frequency rotational modes in solid acids. Therefore, we use ω_{cat} as a descriptor of the lattice dynamic flexibility and the ease of the polyanion group rotations.

We define the rotational flexibility metric based on the standard deviations of the angles characterizing group rotations (*i.e.*, the polar and azimuthal angles, θ and φ, in the internal spherical coordinate system for each group vector, see Section S1 in the ESI†). We take the larger of the standard deviations of these two angles of rotation and show its dependence on the cation phonon band centers of the considered materials in Fig. 3c. The correlation between the proton diffusivity and the cation phonon band centers is shown in Fig. 3d. The majority of compounds with a low cation phonon band center (below about 3.5 THz) show good rotational flexibility, *i.e.* a large standard deviation of θ or φ, along with high proton diffusivity. For these compounds, the standard deviation of rotational angles is generally $\geq 40^\circ$, indicating pronounced rotational excursions. This also means that 3 standard deviations correspond to about 120°, which is comparable to the 109.5° angle of the full tetrahedron rotation of the polyanion groups. Upon analyzing the maximal rotation angles observed during AIMD, a similar partition of compounds was found (Fig. S4, ESI†); *i.e.*, compounds that show full rotation of the polyanion tetrahedral with maximal rotational angles above 109.5° mostly have cation phonon band centers below 3.5 THz. Conversely, the majority of compounds with a high cation phonon band center (above about 3.5 THz) show poor rotational flexibility, with a rotational metric of lower than 40° (in fact, mostly lower than 40° as seen in Fig. 3c), and low diffusivity, indicating that the polyanion group rotation is limited. This correlation holds for all the compounds that we screened, except for a few that we excluded from consideration because the framework cations were partially or fully coordinated with water molecules (*e.g.*, $Nd(H_2O)_2(H_{0.5}SeO_3)_2$ and $Mg(H_2O)_6(SeO_3)$), which block correlated motion between the cation and the polyanion groups. Consequently, these compounds require a different metric to characterize the rotational motion of polyanion groups independent from the framework cations.[62,74]

Combining descriptors of proton transfer and group rotation

Since the Grotthuss mechanism is a two-step process, we considered separate descriptors for each step. One can see that individually each descriptor imposes a necessary but

insufficient condition for achieving a high diffusion coefficient for protons in solid acids. For example, the proton–donor bond length needs to be longer than a certain cut-off d_{OH} for proton transfer to take place (Fig. 2b and d), but this does not guarantee that diffusion will be long-range. Similarly, a low cation phonon band center favors good rotational flexibility, but it does not guarantee that proton transfer will be facile.

Fig. 4 shows a grouping of the simulated proton diffusion coefficients as a function of descriptors of both the proton transfer and the group rotation steps. We see that most of the fast proton conductors ($D_H^{700K} > 10^{-6}$ cm^2 s^{-1}, red data points in Fig. 4a) cluster in the region with a low cation phonon band center ($\lesssim$3.5 THz) and a large initial O–H bond length ($d_{OH} \gtrsim 1.007$ Å). We observe a similar clustering in the ΔpK_a *vs.* ω_{cat} coordinates (Fig. 4b). The chosen cutoffs for ω_{cat} and d_{OH} allow us to separate proton conducting and non-conducting compounds with a low number of false-positive (3) and false-negative (4) cases. By using one descriptor each for proton transfer and for group rotation kinetics, we can predict which materials are expected to show both facile local proton hops and facile group rotation and therefore should be good proton conductors.

In summary, our results show that the length of the proton–donor covalent bond, d_{OH}, and the difference between donor and acceptor acidities, ΔpK_a, are good descriptors of the ease of proton transfer, and the cation phonon band center, ω_{cat}, is a good descriptor of the rotational flexibility of polyanion groups. Therefore, we next use these physically based descriptors to identify novel proton conductors by means of high-throughput computational screening. Between d_{OH} and ΔpK_a, we use the former in the high-throughput screening, as a more facile and structurally sensitive descriptor that we extract directly from the simulated structure in our calculations.

High-throughput screening based on physical descriptors

The screening workflow introduced in Computational methods (Section S1 in the ESI†) is detailed in Fig. 5. After an initial screening of 5207 materials based on various properties (steps I–IV), the dataset contained 874 compounds that possess low electronic conductivity, have hydrogen bonds, and are considered synthesizable. We have applied screening based on the identified descriptors on this data set of 874 compounds. Specifically, we selected materials that possess polyanion groups with a donor–hydrogen bond length, d_{OH}, longer than 1.007 Å (step V) and have a cation with the phonon band center, ω_{cat}, below 3.5 THz (step VI). Application of these criteria eliminated about 84% of materials that were not expected to be fast proton conductors, thus leaving 143 candidates (of which, 112 had unique compositions). The final dataset includes these 143 candidates. For these materials, we performed Machine Learning Force Field accelerated AIMD (MLFF–AIMD)[46–48] simulations to screen proton diffusivities at 650 K (step VII). We provide the complete list of materials, respective descriptors, and computed diffusivities in Table S2 (ESI†). Subsequently (step VIII), we selected the most promising compounds and explored their diffusivities in detail by MD (either AIMD or MLFF–AIMD) as a function of temperature below 650 K.

Before presenting the results of the diffusivity calculations, it is of value to consider the material properties of the 143 candidate conductors (Table S2, ESI†) treated in the final dataset. The majority of solid acids that satisfy the used criteria $d_{OH} > 1.007$ Å and $\omega_{cat} < 3.5$ THz are the Cs, Rb, and K-based ones (about 76%), and the rest are based on other cations including Ag^+, Hg^+, Tl^+, Ba^{2+}, Cd^{2+}, Pb^{2+}, Sr^{2+}, Er^{3+}, U^{6+} and Bi^{x+} (Fig. 6a). As evident in the scatter plot of features of these compounds, Fig. 6a, the d_{OH} values range from 1.007 Å to about 1.2 Å showing no preference across various elements or cation charges. In contrast, the ω_{cat} value broadly depends on the chemical element itself, leading to the formation of clusters of ω_{cat} values around each of Tl, Cs, Rb, Ag, Ba, and K-based compounds. The compound-averaged ω_{cat} values decrease as the effective cation radii increase (see Fig. S5, ESI†). This corroborates

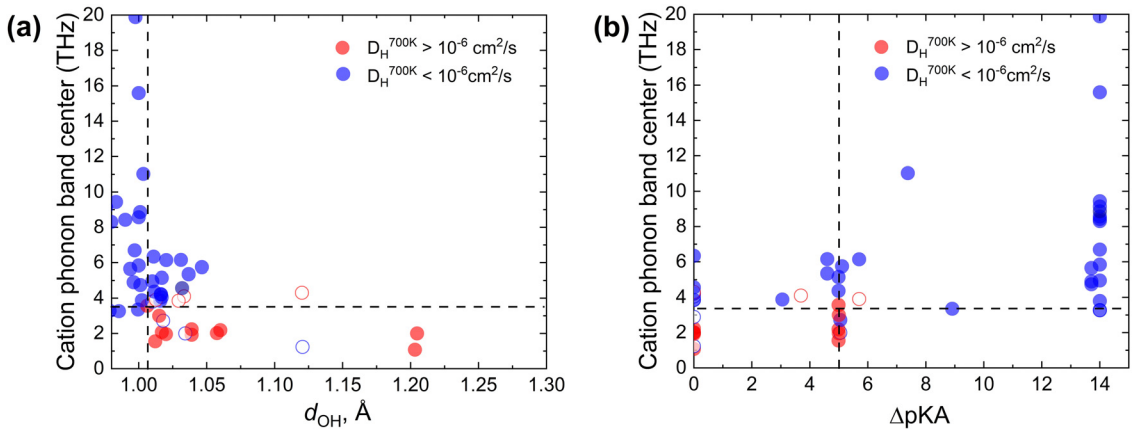

Fig. 4 (a) Scatter plot of D_H as a function of the cation phonon band center ω_{cat} and d_{OH}. Points are grouped/colored according to diffusivities from AIMD simulations at 700 K. Fast ($D_H > 10^{-6}$ cm^2 s^{-1}) proton conductors are shown in red, and slow ($D_H < 10^{-6}$ cm^2 s^{-1}) proton conductors are shown in blue. The clustering of fast proton conductors in the region with $d_{OH} \gtrsim 1.007$ Å and cation phonon band centers $\lesssim$3.5 THz is seen. (b) The same as (a), but plotted in the ω_{cat} *vs.* ΔpK_a coordinates (a similar clustering of fast proton conductors is seen). Open circles highlight the false positive and false negative data points.

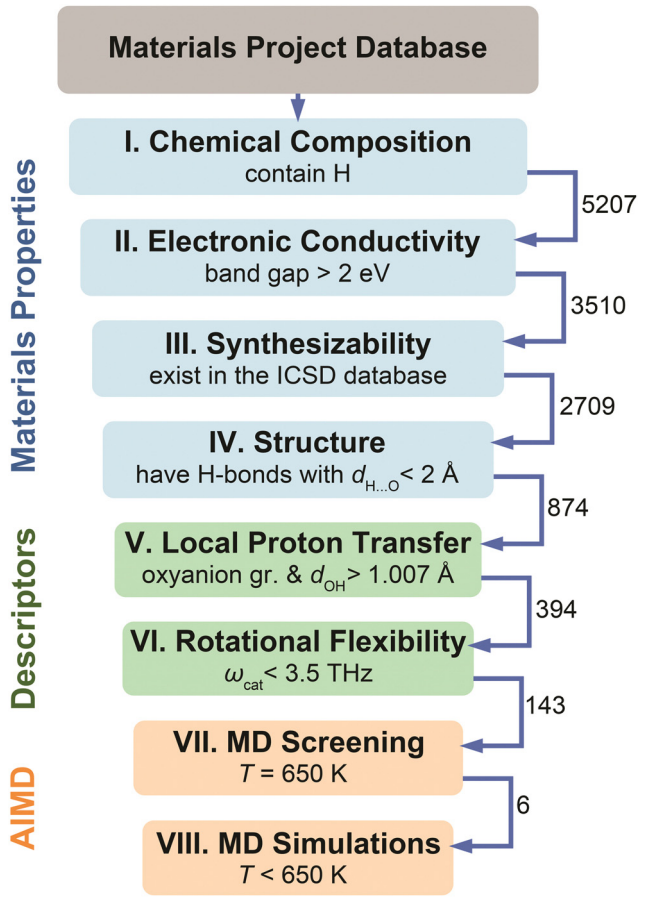

Fig. 5 Flowchart of the high-throughput screening of the Materials Project[44] database based on the materials properties (steps I–IV), the identified physical descriptors (steps V–VI), and MD diffusivities (steps VII–VIII). See Computational methods, Section S1 in the ESI,† for details regarding each step. The numbers near arrows show how many compounds reached the next step.

earlier hypotheses that large cations generally provide an increased lattice flexibility.[19,75] However, as can be seen in Fig. 6a, the cation size alone is not a sufficient condition for quantitatively relating to flexibility; *i.e.*, there is a range of ω_{cat} values for a group of compounds with the same cation. Different crystal structures with the same cation can have different flexibilities reflected with different cation phonon band centers. For example, Cs containing compounds have cation phonon band centers ranging from 1.2 THz to 2.7 THz. We also recognize that some compounds that passed the screening are toxic or radioactive, containing for example, Tl and U, and thus are not desirable for practical applications.

The computed diffusivities of the 143 compounds (from Fig. 6a and Table S2, ESI†) in the final dataset are presented as a histogram in Fig. 6b. About 30 compounds show high conductivity as evaluated at 650 K ($D_H \gtrsim 10^{-6}$ cm^2 s^{-1}; see discussion below regarding compounds with low conductivities). Importantly, our screening procedure finds most of the known Cs, Rb, and K-based compounds with superprotonic transitions, *e.g.*, $K_3H(SeO_4)_2$, $Rb_3H(SeO_4)_2$, $Cs_3H(SeO_4)_2$, $CsHSO_4$, and $CsHSeO_4$,[6,76,77] which satisfy the proposed descriptor criteria and also demonstrate reasonable diffusivity in MD tests (see Table S2, ESI†). We also identify several less known Cs, Rb, and K-based compounds such as $Cs(HF)(H_2PO_4)$, $Rb(H_{2.5}AsO_4)_2$, and $K_4(H_3AsO_4)(HSO_4)_2(SO_4)$ that might be promising proton conductors (Table S2, ESI†).

We were particularly intrigued to find fast proton conductors among solid acids based on "unconventional" cations such as Ag^+, Ba^{2+}, Sr^{2+}, and Er^{3+}. We explored several such compounds using MD simulations as shown in Fig. 7 and summarized in Table 2. Their conductivities reach 10^{-2} S cm^{-1} at 500 K (Table 2), ranging from 10^{-3} to 10^{-1} S cm^{-1} between 400 and 600 K (Fig. 7). For example, $Er(HSO_4)_3$[78] shows 10^{-2} S cm^{-1} at 500 K and $Ag(H_3O)(HSO_4)_2$[79] shows 0.5 mS cm^{-1} at 400 K. The latter solid also supports vehicle diffusion, though it is a minor contribution to diffusion compared to the Grotthuss mechanism. Significantly, the calculated conductivities are higher than or comparable to that of $CsHSO_4$ (mp-1192419, $P2_1/c$ ref. 73) as shown in Fig. 7. To the best of our knowledge, the conductivities of these identified solid acids (Table 2 and Fig. 7) have not been experimentally reported in the literature.

In light of the low number of false positives indicated in Fig. 4, we were surprised that a large number of compounds passed our screening (Fig. 6a) but does not show fast proton diffusion at 650 K (Fig. 6b, Table S2, ESI†). There can be two reasons for this. First is that our screening criteria may be incomplete, and the screening model could be improved to filter out more of the non-conducting compounds by considering other factors, *e.g.*, the spatial arrangement of donor–acceptor sites and/or topology[84] of the hydrogen bonding network. In addition, some compounds have more than one cation, and we have screened based on only the one cation that has the ω_{cat} of <3.5 THz. For example, our dataset contained 40 solid acids that have more than one cation, such as $Ba_2Cd(H_{1.5}PO_4)_4$, $Ba_2CaH_6(PO_4)_4$, and $Ni_3AgH_2(PO_4)_3$, and the great majority of them showed negligible diffusion (Table S2, ESI†). All these compounds had another non-soft cation ($\omega_{cat} > 3.5$ THz), which can constrain the lattice flexibility. This is in agreement with our earlier experimental study that observed no superprotonic transition in $Cs_2Na(HSO_4)_3$ and $CsNa_2(HSO_4)_3$ and suggested that strong Na–O bonds hinder structural flexibility.[75]

A second reason for finding many of the screened compounds (from Fig. 6) with low proton diffusion at 650 K can be the use of the NVT ensemble in our MD simulations. By constraining the cell shape and volume, we do not allow explicit phase transitions (only rearrangements facilitated by temperature, see Fig. S6 and S7, ESI†). This constraint may suppress plausible superprotonic transitions and decrease diffusivity (*e.g.*, the simulated diffusivity of $CsHSO_4$ in Fig. 6 is by one order of magnitude lower than the experimental one,[6] and not every $CsHSO_4$ phase shows high diffusivity, see Table S2, ESI†). On the other hand, the predicted high conductivity does not guarantee that the phase will be stable at the simulated temperatures. For example, we predict triclinic[83] $Ba(H_2PO_4)_2$ to show exceptional conductivity (Fig. 7); however, this phase is

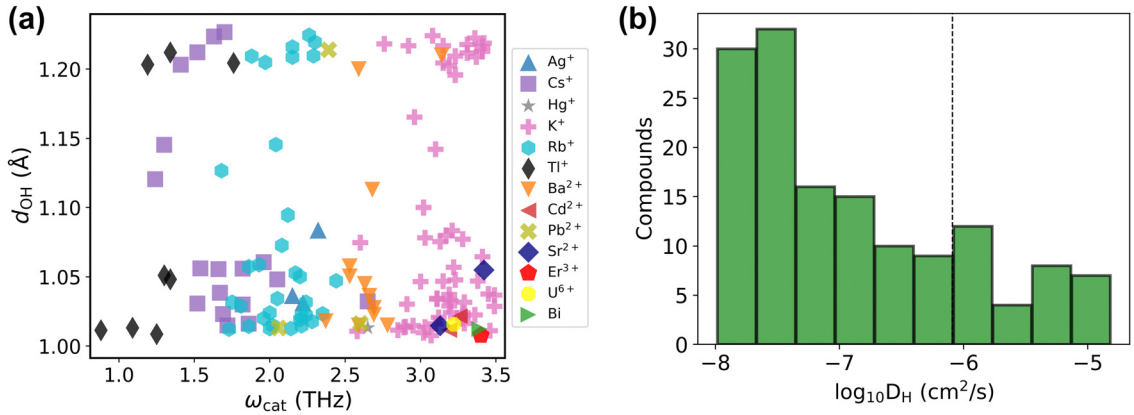

Fig. 6 Final dataset analysis. (a) The final dataset presented as the scatter plot of the maximal d_{OH} *vs.* cation phonon band center ω_{cat}. Different cations are highlighted with different colors (for compounds with multiple cations, the lowest ω_{cat} is plotted). The list of these compounds is provided in Table S2 (ESI†). (b) Histogram of diffusivities of the final dataset computed at 650 K using machine learning force field accelerated AIMD (MLFF–AIMD) simulations. The vertical dashed line marks $D_H \approx 10^{-6}$ cm^2 s^{-1}.

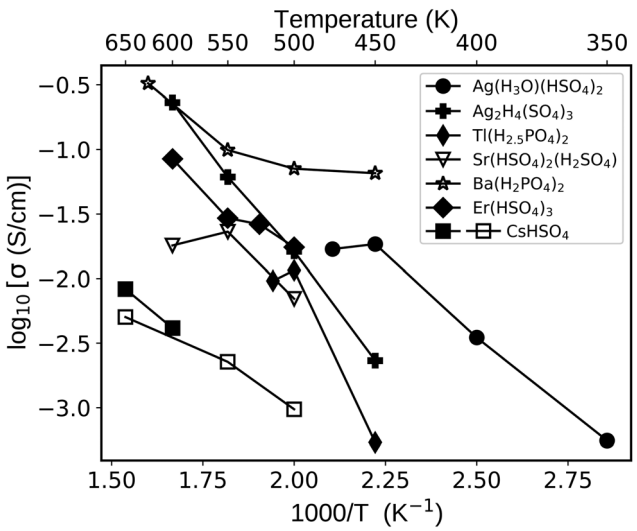

Fig. 7 Proton conductivities of selected solid acids calculated with AIMD (full symbols) and MLFF–AIMD (open symbols). The cell sizes and shapes were constrained to the room temperature (or low temperature) phases as retrieved from the Materials Project database (see Table 2). The simulated $CsHSO_4$ (mp-1192419) conductivity is shown as a baseline (MLFF–AIMD and AIMD demonstrate consistent results; see Section S1 in the ESI† for further details).

Table 2 The list of promising solid acids with non-Cs and non-Rb cations, their Materials Project[44] IDs, respective ICSD[45] IDs, and proton conductivities from our AIMD simulations shown in Fig. 7 (for Ba and Sr compounds, we used MLFF–AIMD). References to the experimental synthesis records from the ICSD are provided (all phases were reported at room temperature, except for the Sr compound reported at 160 K)

Compound	mp-ID	ICSD-ID	Ref.	σ_H (500 K) (mS cm^{-1})
$Ag(H_3O)(HSO_4)_2$[a]	mp-24072	408948	79	17 [@475 K]
$Ag_2H_4(SO_4)_3$[a]	mp-867593	408949	79	16
$Tl(H_{2.5}PO_4)_2$	mp-696762	30509	81	12
$Sr(HSO_4)_2(H_2SO_4)$[a]	mp-757723	404139	82	7
$Ba(H_2PO_4)_2$[b]	mp-706543	2420	83	70
$Er(HSO_4)_3$[a]	mp-24640	408804	78	17

[a] Hygroscopic, requires an inert atmosphere (see corresponding ref.) [b] Meta-stable phase (triclinic) according to ref. 80.

hard to stabilize.[80] The more stable orthorhombic phase does not show high proton conductivity either in experiments[85] or in our simulations (see mp-706400 record in Table S2, ESI†). Likewise, we cannot predict whether melting precedes[86,87] a superprotonic transition. Another limitation of the NVT ensemble is the assumption of a fixed stoichiometry and composition. However, in practice, proton conductivity in these compounds depends on the humidity and temperature, *e.g.*, causing dehydration[88–90] or disproportionation,[91] both of which can affect conductivity. These examples of the behavior of $Ba(H_2PO_4)_2$ show that our MD diffusivities are influenced by the NVT ensemble, and explicit modelling of phase transitions would be desirable, yet challenging at present. Nevertheless, the calculated MD diffusivities (Table 2 and Fig. 7) remain strong indicators of fast proton conductivity in these compounds.

Our screening was limited to the Materials Project[44] database (about 154 thousand materials), yet more conductors may be identified by screening larger databases such as ICSD[45] (about 281 thousand compounds), OQMD[92] (about 1 million compounds), or GNoME (about 2.2 million compounds).[93] Rapid development of databases[93] and inverse materials design methods[38,94–97] presents an opportunity for such descriptor-based search of fast proton conductors with desirable properties (low T_{sp}, high chemical and thermal stabilities, *etc.*). In this regard, it is promising that our screening, albeit limited to the MP database, could uncover solid acids with less explored chemistries, demonstrating potential for screening of larger datasets[93] in future studies.

The established physical descriptors could be applied to other classes of proton conductors. However, such an expansion of the method requires considering the specifics of proton transfer and the Grotthuss reorganization of the environment,

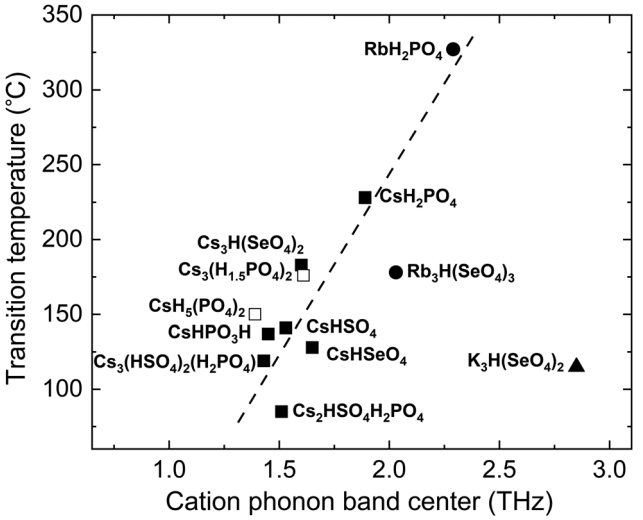

Fig. 8 Experimental superprotonic transition temperature, T_{sp}, of solid acids from the literature *vs.* the average cation phonon band center, ω_{cat}, which is calculated in this work for each of those compounds. Open squares represent the melting temperatures of compounds that do not show superprotonic transition (*i.e.*, melt below an accessible T_{sp}). The trend line is the guide to the eye. Data points for Cs-based compounds[77,87,90,100–106] are squares, Rb-based compounds[77,103] are circles, and the K-based[77] solid acid is shown as a triangle.

and the chemistry and structure in each class of material, resulting in different quantitative relations of the descriptors to the conductivity. Possible classes include but are not limited to perovskites and other ceramic oxides[22] as well as polymer conductors.[24] For example, in metal oxides, while we do not expect significant rotations of the metal–oxygen polyhedra (as opposed to the rotations of polyanion groups in solid acids), we can expect that the lattice flexibility can still play a role by dynamically bringing closer donor–acceptor pairs assisted by different phonon modes at finite temperatures. Similar design principles, such as searching for complex compounds with a continuous hydrogen bonding network as in the newly discovered $ZrH_5(PO_4)_3$ solid acid,[98] provide another promising route to find fast, solid-state proton conductors.

Superprotonic transition temperature and its correlation with cation phonon band centers

For superprotonic solid acids, it is imperative to know not only whether a high conductivity phase exists, but also the temperature above which the high conductivity phase is stable, *i.e.*, the superprotonic transition temperature, T_{sp}. It is desirable to obtain materials with relatively low T_{sp} such that the superprotonic phase is encountered prior to melting or dehydration.[99] To address this, we explored correlations between T_{sp} and the descriptor of group rotation flexibility. The rationale is that the polyanion sublattice "rotationally melts" in the superprotonic phase; therefore, T_{sp} should correlate with the rotational flexibility and descriptors thereof.

We found that the experimentally measured T_{sp} in a comprehensive set of Cs-containing superprotonic solid acids correlates with the calculated cation phonon band center, Fig. 8. For compounds with multiple, inequivalent Cs sites, which display distinct band centers for each unique Cs (*e.g.*, Cs_2HSO_4-H_2PO_4 [1.43 THz and 1.60 THz] and $Cs_3(HSO_4)_2(H_2PO_4)$ [1.36 THz, 1.50 THz, 1.81 THz]), we used the average frequencies from different cation sites. The greater the flexibility of the cation framework under ambient conditions, the lower the temperature required for transitioning to the superprotonic phase. This observed correlation implies that the superprotonic transition in these materials is indeed related to the rotational flexibility of polyanion groups. However, the rotational flexibility may alternatively lead to a complete melting transition, as is the case for two of the nine compounds considered, and additional criteria will be required to distinguish between the type of transition that occurs. Significantly, two identified Rb superprotonic compounds fall along the same trend line with the Cs compounds, reflecting chemical similarity between these species. The representative K compound indicated in Fig. 8 deviates from the trend line. Because there are a very limited number of experimental reports of superprotonic phase transition in solid acids that do not include Cs, the possibilities for elucidating the specific role of the cation species are limited, though cation mass may directly play a role by affecting the force constants (Fig. S8, ESI†).

Dependence of T_{sp} on the softness of the cation framework underscores the importance of lattice flexibility. A large cation size alone is not a sufficient quantitative indicator of increased lattice flexibility and the lowering of T_{sp}. As seen in Fig. 8, even for solid acids with the same framework cation, Cs, T_{sp} varies more than 100 °C and the ω_{cat} varies by about 1 THz. Explicit quantification of lattice flexibility (*i.e.*, through the cation phonon band center, as done here) appears to be a more useful predictor of T_{sp}. Since the correlation between ω_{cat} and T_{sp} is not precise, consideration of other factors, for example, bonding network topology, inequivalence of cation sites and the role of multiple phonon band centers, and disparity of the cation masses, may provide further insights into the complete set of factors that control T_{sp}.

Conclusion

In this work, we have established quantitative conditions for physical descriptors that enable high proton conductivity in solid acids. The physical descriptors correspond to the two key steps of proton transport based on the Grotthuss mechanism. The ease of proton transfer between the donor and acceptor sites depends on the donor–proton (O–H) bond strength, inversely related to the bond length d_{OH}; *i.e.*, larger d_{OH} leads to easier local proton transfer. Similarly, the smaller the difference in pK_a of the donor and acceptor sites, the easier the local proton transfer. The rotational flexibility of the polyanion groups depends on the phonon band center of the framework cation sublattice, ω_{cat}; *i.e.*, lower ω_{cat} leads to a softer cation framework, a more flexible lattice and easier group rotations. The cation phonon band center also correlates with the experimentally reported temperatures of superprotonic

transition. This finding suggests that increasing the lattice flexibility to facilitate polyanion group rotations can decrease T_{sp} and help achieve high proton conductivity at lower temperatures. Our work provides guidance on how to quantify the rotational flexibility and T_{sp} based on the lattice dynamics features for arbitrary compositions. The model for descriptors of proton conductivity and T_{sp} can be further improved in the future to include other possible factors, such as the network topology of hydrogen bonds and structural constraints on the group rotations.

Based on the identified descriptors, we screened the Materials Project[44] database and revealed potential solid acid proton conductors. The well-known fast proton conductors with Cs^+, Rb^+, and K^+ framework cations satisfy our descriptor criteria. We also found prospective fast proton conductors with "unconventional" cations for solid acid proton conductors. These include Ag^+, Ba^{2+}, Sr^{2+} and Er^{3+} framework cations. AIMD simulations indicate that these compounds can possess proton conductivities that are higher than that of $CsHSO_4$. This finding of "unconventional" chemistries suggests that there is an opportunity to reveal more solid acid proton conductors by screening larger materials databases. We expect that the available compositional space of proton-conducting solid acids is broader than what has been used so far. We believe that our results will inspire further studies to investigate larger materials datasets and implement novel proton-conducting solid acids for different applications from energy conversion to electronic devices.

Data availability

The data supporting this article have been included as part of the ESI.†

Conflicts of interest

There are no conflicts to declare.

Acknowledgements

This work was primarily supported by the Hydrogen in Information and Energy Sciences (HEISs) Center, an Energy Frontier Research Center funded by the U.S. Department of Energy, Office of Science, Basic Energy Sciences under Award # DE-SC0023450. P.Ž. thanks the Knut and Alice Wallenberg Foundation scholarship program for supporting part of his postdoctoral studies at the Massachusetts Institute of Technology. L.W. was supported by a Graduate Research Fellowship from the US National Science Foundation (NSF). G. X. was supported by the NSF Grant No. OAC 2118201. The authors acknowledge the Texas Advanced Computing Center (TACC) at The University of Texas at Austin for providing the HPC resources on the Frontera supercomputer (allocation # DMR20012) that have contributed to the first principles simulations and MD results reported within this work.

References

1 C. Duan, J. Tong, M. Shang, S. Nikodemski, M. Sanders, S. Ricote, A. Almansoori and R. O'Hayre, *Science (1979)*, 2015, **349**, 1321–1326.
2 S. Choi, C. J. Kucharczyk, Y. Liang, X. Zhang, I. Takeuchi, H.-I. Ji and S. M. Haile, *Nat. Energy*, 2018, **3**, 202–210.
3 H. An, H. W. Lee, B. K. Kim, J. W. Son, K. J. Yoon, H. Kim, D. Shin, H. Il Ji and J. H. Lee, *Nat. Energy*, 2018, **3**, 870–875.
4 H. Ding, W. Wu, C. Jiang, Y. Ding, W. Bian, B. Hu, P. Singh, C. J. Orme, L. Wang, Y. Zhang and D. Ding, *Nat. Commun*, 2020, **11**, 1907.
5 F. Liu, H. Deng, H. Ding, P. Kazempoor, B. Liu and C. Duan, *Joule*, 2023, **7**, 1308–1332.
6 S. M. Haile, D. A. Boysen, C. R. I. Chisholm and R. B. Merie, *Nature*, 2001, **410**, 910–913.
7 D. A. Boysen, T. Uda, C. R. I. Chisholm and S. M. Haile, *Science (1979)*, 2004, **303**, 68–70.
8 T. Uda, D. A. Boysen, C. R. I. Chisholm and S. M. Haile, *Electrochem. Solid-State Lett.*, 2006, **9**, A261–A264.
9 D. K. Lim, A. B. Plymill, H. Paik, X. Qian, S. Zecevic, C. R. I. Chisholm and S. M. Haile, *Joule*, 2020, **4**, 2338–2347.
10 X. Wu, J. J. Hong, W. Shin, L. Ma, T. Liu, X. Bi, Y. Yuan, Y. Qi, T. W. Surta, W. Huang, J. Neuefeind, T. Wu, P. A. Greaney, J. Lu and X. Ji, *Nat. Energy*, 2019, **4**, 123–130.
11 L. Yan, J. Huang, Z. Guo, X. Dong, Z. Wang and Y. Wang, *ACS Energy Lett.*, 2020, 685–691.
12 Z. Shao, A. Huang, C. Ming, J. Bell, P. Yu, Y.-Y. Sun, L. Jin, L. Ma, H. Luo, P. Jin and X. Cao, *Nat. Electron.*, 2022, **5**, 1–8.
13 A. J. Tan, M. Huang, C. O. Avci, F. Büttner, M. Mann, W. Hu, C. Mazzoli, S. Wilkins, H. L. Tuller and G. S. D. Beach, *Nat. Mater.*, 2019, **18**, 35–41.
14 M. Huang, M. U. Hasan, K. Klyukin, D. Zhang, D. Lyu, P. Gargiani, M. Valvidares, S. Sheffels, A. Churikova, F. Büttner, J. Zehner, L. Caretta, K. Y. Lee, J. Chang, J. P. Wang, K. Leistner, B. Yildiz and G. S. D. Beach, *Nat. Nanotechnol.*, 2021, **16**, 981–988.
15 X. Yao, K. Klyukin, W. Lu, M. Onen, S. Ryu, D. Kim, N. Emond, I. Waluyo, A. Hunt, J. A. del Alamo, J. Li and B. Yildiz, *Nat. Commun.*, 2020, **11**, 3134.
16 M. Onen, N. Emond, J. Li, B. Yildiz and J. A. Del Alamo, *Nano Lett.*, 2021, **21**, 6111–6116.
17 M. Onen, N. Emond, B. Wang, D. Zhang, F. M. Ross, J. Li, B. Yildiz and J. A. del Alamo, *Science (1979)*, 2022, **377**, 539–543.
18 M. Huang, M. Schwacke, M. Onen, J. del Alamo, J. Li and B. Yildiz, *Adv. Mater.*, 2022, 2205169.
19 K.-D. Kreuer, *Chem. Mater.*, 1996, **8**, 610–641.
20 T. Norby, *Solid State Ionics*, 1999, **125**, 1–11.
21 L. Malavasi, C. A. J. Fisher and M. S. Islam, *Chem. Soc. Rev.*, 2010, **39**, 4370–4387.
22 Y. Meng, J. Gao, Z. Zhao, J. Amoroso, J. Tong and K. S. Brinkman, *J. Mater. Sci.*, 2019, **54**, 9291–9312.
23 K. Biradha, A. Goswami, R. Moi and S. Saha, *Dalton Trans.*, 2021, **50**, 10655–10673.

24 Y. Sone, P. Ekdunge and D. Simonsson, *J. Electrochem. Soc.*, 1996, **143**, 1254–1259.
25 A. I. Baranov, *Crystallogr. Rep.*, 2003, **48**, 1012–1037.
26 K. D. Kreuer, *Solid State Ionics*, 1997, **94**, 55–62.
27 Y. Zhang, X. He, Z. Chen, Q. Bai, A. M. Nolan, C. A. Roberts, D. Banerjee, T. Matsunaga, Y. Mo and C. Ling, *Nat. Commun.*, 2019, **10**, 1–7.
28 L. Kahle, A. Marcolongo and N. Marzari, *Energy Environ. Sci.*, 2020, **13**, 928–948.
29 S. Muy, J. Voss, R. Schlem, R. Koerver, S. J. Sedlmaier, F. Maglia, P. Lamp, W. G. Zeier and Y. Shao-Horn, *iScience*, 2019, **16**, 270–282.
30 A. D. Sendek, E. D. Cubuk, E. R. Antoniuk, G. Cheon, Y. Cui and E. J. Reed, *Chem. Mater.*, 2019, **31**, 342–352.
31 B. He, P. Mi, A. Ye, S. Chi, Y. Jiao, L. Zhang, B. Pu, Z. Zou, W. Zhang, M. Avdeev, S. Adams, J. Zhao and S. Shi, *Acta Mater*, 2021, **203**, 116490.
32 B. He, S. Chi, A. Ye, P. Mi, L. Zhang, B. Pu, Z. Zou, Y. Ran, Q. Zhao, D. Wang, W. Zhang, J. Zhao, S. Adams, M. Avdeev and S. Shi, *Sci Data*, 2020, **7**, 1–14.
33 K. J. Jun, Y. Sun, Y. Xiao, Y. Zeng, R. Kim, H. Kim, L. J. Miara, D. Im, Y. Wang and G. Ceder, *Nat. Mater.*, 2022, **21**, 924–931.
34 C. López, A. Emperador, E. Saucedo, R. Rurali and C. Cazorla, *Mater. Horiz.*, 2023, **10**, 1757–1768.
35 M. Matsubara, A. Suzumura, N. Ohba and R. Asahi, *Commun. Mater.*, 2020, **1**, 1–6.
36 P. Priya and N. R. Aluru, *npj Comput. Mater.*, 2021, **7**, 1–12.
37 A. D. Sendek, Q. Yang, E. D. Cubuk, K. A. N. Duerloo, Y. Cui and E. J. Reed, *Energy Environ. Sci.*, 2017, **10**, 306–320.
38 K. E. Willcox, O. Ghattas and P. Heimbach, *Nat. Comput. Sci.*, 2021, **1**, 166–168.
39 J. Hyodo, K. Tsujikawa, M. Shiga, Y. Okuyama and Y. Yamazaki, *ACS Energy Lett.*, 2021, **6**, 2985–2992.
40 M. S. Islam, S. Wang, A. M. Nolan and Y. Mo, *Chem. Mater.*, 2021, **33**, 8278–8288.
41 M. S. Islam, S. Wang, A. T. Hall and Y. Mo, *Chem. Mater.*, 2022, **34**, 5938–5948.
42 N. Bork, N. Bonanos, J. Rossmeisl and T. Vegge, *Phys. Rev. B: Condens. Matter Mater. Phys.*, 2010, **82**, 014103.
43 Y. Yamazaki, A. Kuwabara, J. Hyodo, Y. Okuyama, C. A. J. Fisher and S. M. Haile, *Chem. Mater.*, 2020, **32**, 7292–7300.
44 A. Jain, S. P. Ong, G. Hautier, W. Chen, W. D. Richards, S. Dacek, S. Cholia, D. Gunter, D. Skinner, G. Ceder and K. A. Persson, *APL Mater.*, 2013, **1**, 011002.
45 A. Belkly, M. Helderman, V. L. Karen and P. Ulkch, *Acta Crystallogr., Sect. B: Struct. Sci.*, 2002, **58**, 364–369.
46 R. Jinnouchi, J. Lahnsteiner, F. Karsai, G. Kresse and M. Bokdam, *Phys. Rev. Lett.*, 2019, **122**, 225701.
47 R. Jinnouchi, F. Karsai and G. Kresse, *Phys. Rev. B*, 2019, **100**, 14105.
48 R. Jinnouchi, F. Karsai, C. Verdi, R. Asahi and G. Kresse, *J. Chem. Phys.*, 2020, **152**, 234102.
49 C. Dreßler and D. Sebastiani, *Phys. Chem. Chem. Phys.*, 2020, **22**, 10738–10752.
50 T. Steiner, *Angew. Chem., Int. Ed.*, 2002, **41**, 48–76.
51 M. Ichikawa, *Acta Crystallogr., Sect. B: Struct. Crystallogr. Cryst. Chem.*, 1978, **34**, 2074–2080.
52 D. Borgis, G. Tarjus and H. Azzouz, *J. Chem. Phys.*, 1992, **97**, 1390–1400.
53 W. Münch, G. Seifert, K. D. Kreuer and J. Maier, *Solid State Ionics*, 1997, **97**, 39–44.
54 M. F. Hoedl, A. Chesnokov, D. Gryaznov, R. Merkle, E. A. Kotomin and J. Maier, *J. Mater. Chem. A*, 2023, **11**, 6336–6348.
55 D. A. Evans and D. H. Ripin, ''pKa's of Inorganic and Oxo-Acids,'' can be found under **https://www.wanglab.chem.pitt.edu/wp-content/uploads/2017/09/Evans-D.-A.-Ripin-D.-H.-The-Evans-pKa-Table-Harvard-2006.pdf**.
56 C. J. Peacock and G. Nickless, *Z. Naturforsch., A: Phys. Sci.*, 1969, **24**, 245–247.
57 ''Engineering ToolBox, (2017), Inorganic Acids and Bases – pKa Values.,'' can be found under **https://www.engineeringtoolbox.com/pKa-inorganic-acid-base-hydrated-metal-ion-monoprotic-diprotic-triprotic-tetraprotic-d_1950.html**.
58 W. M. Haynes, ed., *CRC Handbook of Chemistry and Physics*, Taylor & Francis, 2014.
59 T. T. Mayeshiba and D. D. Morgan, *Solid State Ionics*, 2016, **296**, 71–77.
60 C. F. Dickens, J. H. Montoya, A. R. Kulkarni, M. Bajdich and J. K. Nørskov, *Surf. Sci.*, 2019, **681**, 122–129.
61 T. S. Bjørheim, M. F. Hoedl, R. Merkle, E. A. Kotomin and J. Maier, *J. Phys. Chem. C*, 2020, **124**, 1277–1284.
62 M. T. Dove, *Philos. Trans. R. Soc., A*, 2019, 377, DOI: **10.1098/RSTA.2018.0222**.
63 S. Muy, J. C. Bachman, L. Giordano, H. H. Chang, D. L. Abernathy, D. Bansal, O. Delaire, S. Hori, R. Kanno, F. Maglia, S. Lupart, P. Lamp and Y. Shao-Horn, *Energy Environ. Sci.*, 2018, **11**, 850–859.
64 X. Li and N. A. Benedek, *Chem. Mater.*, 2015, **27**, 2647–2652.
65 A. Torayev, L. Sperrin, M. A. Gomez, J. A. Kattirtzi, C. Merlet and C. P. Grey, *J. Phys. Chem. C*, 2020, **124**, 16689–16701.
66 T. Itakura, H. Matsui, T. Tada, S. Kitagawa, A. Demessence and S. Horike, *Chem. Sci.*, 2020, **11**, 1538–1541.
67 V. Korostelev, J. Wagner and K. Klyukin, *J. Mater. Chem. A*, 2023, **11**, 23576–23588.
68 J. C. Maxwell, *London, Edinburgh Dublin Philos. Mag. J. Sci.*, 1864, **27**, 294–299.
69 R. P. Bell, *Proc. R. Soc. London*, 1936, **154**, 414–429.
70 M. G. Evans and M. Polanyi, *Trans. Faraday Soc.*, 1936, **32**, 1333–1360.
71 A. I. Baranov, V. P. Khiznichenko and L. A. Shuvalov, *Ferroelectrics*, 1989, **100**, 135–141.
72 A. I. Baranov, L. A. Shuvalov and N. M. Shchagina, *JETP Lett.*, 1982, **36**, 459–462.
73 K. Itoh, T. Ukeda, T. Ozaki and E. Nakamura, IUCr, *Acta Crystallogr.*, 1990, **C46**, 358–361.
74 M. T. Dove, J. Du, Z. Wei, D. A. Keen, M. G. Tucker and A. E. Phillips, *Phys. Rev. B*, 2020, **102**, 094105.
75 C. R. I. Chisholm, L. A. Cowan and S. M. Haile, *Chem. Mater.*, 2001, **13**, 2909–2912.
76 A. Goñi-Urtiaga, D. Presvytes and K. Scott, *Int. J. Hydrogen Energy*, 2012, **37**, 3358–3372.

77 D. Yi, S. Sanghvi, C. P. Kowalski and S. M. Haile, *Chem. Mater.*, 2019, **31**, 9807–9818.
78 M. S. Wickleder, *Z. Anorg. Allg. Chem.*, 1998, **624**, 1347–1354.
79 A. Stiewe, E. Kemnitz and S. Troyanov, *Z. Anorg. Allg. Chem.*, 1999, **625**, 329–335.
80 B. Prelesnik, R. Herak, M. Čurić and I. Krstanović, *Acta Crystallogr.*, 1978, **34**, 76–78.
81 Y. Oddon, J.-R. Vignalou, A. Tranquard and G. Pèpe, *Acta Crystallogr.*, 1978, **34**, 3510–3514.
82 C. Werner, E. Kemnitz, H. Worzala and S. Trojanov, *Z. Naturforsch., B: J. Chem. Sci.*, 1996, **51**, 952–958.
83 J. D. Gilbert and P. G. Lenhert, *Acta Crystallogr.*, 1978, **34**, 3309–3312.
84 K. S. Gomez-Haibach and M. A. Gomez, *J. Phys. Chem. B*, 2023, **127**, 9258–9266.
85 I. N. Bagryantseva and V. G. Ponomareva, *Inorg. Mater.*, 2018, **54**, 366–373.
86 S. Chandrasekhar, R. Shashidhar and N. Tara, *Mol. Cryst. Liq. Cryst.*, 1970, **10**, 337–358.
87 G. V. Lavrova, E. B. Burgina, A. A. Matvienko and V. G. Ponomareva, *Solid State Ionics*, 2006, **177**, 1117–1122.
88 S. M. Haile, C. R. I. Chisholm, K. Sasaki, D. A. Boysen and T. Uda, *Faraday Discuss.*, 2006, **134**, 17–39.
89 Y. K. Taninouchi, T. Uda, Y. Awakura, A. Ikeda and S. M. Haile, *J. Mater. Chem.*, 2007, **17**, 3182–3189.
90 A. Ikeda and S. M. Haile, *Solid State Ionics*, 2012, **213**, 63–71.
91 L. A. Cowan, R. M. Morcos, N. Hatada, A. Navrotsky and S. M. Haile, *Solid State Ionics*, 2008, **179**, 305–313.
92 S. Kirklin, J. E. Saal, B. Meredig, A. Thompson, J. W. Doak, M. Aykol, S. Rühl and C. Wolverton, *NPJ Comput Mater*, 2015, **1**, 15010.
93 A. Merchant, S. Batzner, S. S. Schoenholz, M. Aykol, G. Cheon and E. D. Cubuk, *Nature*, 2023, **624**, 80–85.
94 B. Sanchez-Lengeling and A. Aspuru-Guzik, *Science (1979)*, 2018, **361**, 360–365.
95 V. Fung, J. Zhang, G. Hu, P. Ganesh and B. G. Sumpter, *npj Comput. Mater.*, 2021, **7**, 200.
96 Z. Ren, S. I. P. Tian, J. Noh, F. Oviedo, G. Xing, J. Li, Q. Liang, R. Zhu, A. G. Aberle, S. Sun, X. Wang, Y. Liu, Q. Li, S. Jayavelu, K. Hippalgaonkar, Y. Jung and T. Buonassisi, *Matter.*, 2022, **5**, 314–335.
97 M. A. Q. Microsoft Research AI4Science, **https://arxiv.org/abs/2311.07361**, 2023.
98 S. Fop, R. Vivani, S. Masci, M. Casciola and A. Donnadio, *Angew. Chem.,– Int. Ed.*, 2023, **62**, e2022184.
99 S. Chandrasekhar, R. Shashidhar and N. Tara, *Mol. Cryst. Liq. Cryst.*, 1970, **10**, 337–358.
100 Z. Jiráak, M. Dlouhá, S. Vratislav, A. M. Balagurov, A. I. Beskrovnyi, V. I. Gordelii, I. D. Datt and L. A. Shwalov, *Phys. Status Solidi A*, 1987, **100**, K117–K122.
101 S. M. Haile, G. Lentz, K. D. Kreuer and J. Maier, *Solid State Ionics*, 1995, **77**, 128–134.
102 M. A. Zakharov, S. I. Troyanov and E. Kemnitz, *Z. Kristallogr.*, 2001, **216**, 172–175.
103 D. A. Boysen, S. M. Haile, H. Liu and R. A. Secco, *Chem. Mater.*, 2003, **15**, 727–736.
104 S. Sanghvi and S. M. Haile, *Solid State Ionics*, 2020, **349**, 115291.
105 C. R. I. Chisholm, R. B. Merle, D. A. Boysen and S. M. Haile, *Chem. Mater.*, 2002, **14**, 3889–3893.
106 C. R. I. Chisholm and S. M. Haile, *Solid State Ionics*, 2000, **136–137**, 229–241.

Electronic Supplementary Material (ESI) for Energy & Environmental Science.

Supporting Information

Uncovering Fast Solid-Acid Proton Conductors Based on Dynamics of Polyanion Groups and Proton Bonding Strength

Pjotrs Žguns[1*], Konstantin Klyukin[1,3*], Louis S. Wang[4], Grace Xiong[4], Ju Li[1,2], Sossina M. Haile[4], Bilge Yildiz[1,2,#]

[1] *Department of Materials Science and Engineering, Massachusetts Institute of Technology, 77 Massachusetts Avenue, Cambridge, Massachusetts 02139, USA*

[2] *Department of Nuclear Science and Engineering, Massachusetts Institute of Technology, 77 Massachusetts Avenue, Cambridge, Massachusetts 02139, USA*

[3] *Department of Materials Engineering, Auburn University, Auburn, Alabama 36849, USA*

[4] *Department of Materials Science and Engineering, Northwestern University, Evanston, IL 60208, USA*

* *These authors contributed equally to this work*

\# byildiz@mit.edu

Table of Contents

Section S1. Computational Methods

Initial and Final Datasets

Initial dataset to identify strong descriptors of proton conductivity: We created an initial dataset to identify correlations between the proposed descriptors and the calculated proton diffusivities (see AIMD simulations below). These compounds were selected from the Materials Project database, with criteria imposed on (*I*) chemical composition, (*II*) electronic band gap, (*III*) synthesizability/phase stability, and *(IV*) structure (hydrogen bonding), as described below (see Screening workflow). To keep the computational cost of AIMD simulations manageable, we applied tight criteria in steps (*II*) and (*III*), reducing the pool of materials to about a hundred. The great majority of thus selected compounds contained oxygen; the small fraction of compounds that had no oxygen (e.g., ZrF_4NH_3, AlF_4NH_4) was excluded for the sake of dataset coherence. Further, we excluded compounds that had no cations (for the list of cations, see step (*VI*)).

The initial dataset consisted of 88 compounds (Table S1). The most of compounds (49) were solid acids with SO_4, PO_4, ClO_4, SeO_3 or other polyanion groups; these included well-known solid-acids such as $CsHSO_4$ and $CsH_5(PO_4)_2$, as well less-known compounds such as $CaHSO_4(H_2SO_4)$, $Er(H_2O)(ClO_4)_3$, $(NH_4)(ReO_4)$, $Mg(H_2O)_6(BrO_3)$, etc. The initial dataset also included compounds (28) that do not have any monomeric groups but rather have oligomeric or polymeric groups such as P_2O_7 (e.g., $CaP_2H_2O_7$) or B_nO_m (e.g., $Ba_3B_6H_2O_{13}$), and compounds (11) that consist solely of water, fluorine or hydroxyl groups (e.g., $Ba(H_2O)(OH)_2$, $ZrF_4(H_2O)_3$). Since such compounds do not have groups that could actively rotate, we excluded them from the analysis of group rotation (see footnotes in Table S1), however we retained them for the analysis of proton transfer as it may still occur. These 39 compounds did not show any significant proton diffusion unless they were completely melted in AIMD simulations, and we therefore excluded such compounds in the final screening (see Final dataset and Screening workflow).

To assess the proton conductivity of the selected materials, we carried out AIMD simulations at elevated temperatures to compute proton diffusivities. Molten compounds (e.g., those having a substantial diffusion of ions other than protons) were excluded from analysis (see Table S1). For 15 of the selected compounds, the mean-square displacement (MSD) analysis of the AIMD trajectories at 700 K revealed a significant proton diffusion characterized by a near-linear MSD growth, while other investigated materials have not demonstrated appreciable diffusion.

Final dataset to screen for fast proton conductors: To identify potential proton conductors based on our identified descriptors, we expanded the number of materials considered by loosening the criteria in steps (*I*), (*II*), and (*III*), while maintaining step (*IV*). We then screened this larger set of candidates by applying criteria determined from the descriptors of proton transfer and group rotation in steps (*V*) and (*VI*), respectively, as described in detail below. The final dataset included 143 solid acids (Table S2). We further explored the proton diffusivities of these materials by running MD simulations as follows. First, in step (*VII*) we ran machine learning force-fields (MLFF) which were trained on-the-fly during AIMD simulations (MLFF–AIMD), as implemented

in the VASP code. MLFF–AIMD simulations were run at 650 K to filter out poor conductors. Finally, we ran AIMD (or MLFF–AIMD) for several selected compounds and explored their proton diffusivities at various temperatures. For this analysis, we specifically selected solid acids with less common cations such as Ag, Sr, Ba, Er, and omitted more common solid acids with Cs, Rb, K cations to reduce the computational cost. However, for the sake of comparison we calculated proton conductivity of $CsHSO_4$ (mp-1192419) to compare the calculated conductivities of non-Cs compounds with that of $CsHSO_4$.

Screening workflow

I. Chemical composition. We considered only materials that already have hydrogen in their chemical formula. For the initial dataset, we excluded compounds with other small cations (Li^+, Na^+, K^+) that could lower the proton transference number, however this restriction was not applied for the final screening. For the initial dataset, we also excluded compounds that do not have oxygen in their chemical formula at this step (for the final dataset, we applied similar criterion in step (*V*)).

II. Electronic band gap. To minimize plausible electronic conductivity, we filtered out materials with a low band gap. We used $E_g > 4$ eV criterion for the initial dataset to keep the number of materials bearable for AIMD. We used $E_g > 2$ eV criterion for the final dataset to include more potential conductors. The band gaps were retrieved from the Materials Project database[1].

III. Synthesizability/*Phase stability*. The initial and final datasets consisted of synthesizable compounds that are reported in the ICSD database[53]. The respective ICSD identifiers were retrieved from the Materials Project database[1]. For the initial dataset, we also applied criterion on the phase stability, i.e., the convex hull energy ($E_{hull} \leq 5$ meV/atom), which was also retrieved from the Materials Project database[1].

IV. Structure. Only compounds possessing D–H…A hydrogen bonds (at least one) were included in the datasets (we applied $d_{H...A} < 2$ Å cut-off). For simplicity, and since polyanion groups may rotate, we set no further restrictions on the number of bonds or their topology.

V. Descriptors of proton transfer. We used the maximal O–H covalent bond length observed in compound, d_{OH}, as a descriptor (it was calculated for the structure as retrieved from the Material Project database). We included only compounds that have (at least one) $d_{OH} > 1.007$ Å belonging to the O–H…O fragments, where either or both O atoms belong to the monomeric oxyanion group, $H_zXO_n^{m-}$; the cut-off of 2 Å was used to identify XO bonds and thus XO_n groups. This allowed us to exclude compounds that have only groups with low rotational flexibility such as P_2O_7, but to include compounds with H_2O/H_3O^+ as units in the hydrogen bonded network. In this step we also excluded compounds that have H_2 molecules or lone H atoms in their structures as retrieved from the Materials Project[1] database. The justification of the chosen cut-off value for d_{OH} is provided in the Results and Discussion section.

VI. Descriptors of group rotation. We used the average cation phonon band center, ω_{cat}, as a descriptor. For the final dataset, we selected compounds that have cations with $\omega_{cat} < 3.5$ THz (the justification for choosing this cut-off value is provided in the Results and Discussion section). For

compounds with multiple cations, we selected the compound if this criterion was satisfied by any of the cations. For the screening purposes, we broadly defined cation as any element excluding the following: halogens, O, S, Se, Te, Po, N, P, As, Sb, C, Si, Ge, B, H, and noble gases. Compounds that have no cations were also excluded.

VII. MD Screening. We computed proton diffusivities of 143 compounds (final dataset) at 650 K, by running MLFF–AIMD simulations (see the AIMD subsection below).

VIII. MD Simulations. We computed proton diffusivities of selected compounds at various temperatures by AIMD (or MLFF–AIMD) simulations (see the AIMD subsection below).

AIMD simulations of proton diffusion

Proton diffusivities were assessed with *Ab Initio* Molecular Dynamics (AIMD) simulations using the Projector Augmented Wave method[2,3] and Perdew–Burke–Ernzerhof (PBE) exchange-correlation functional[4,5] implemented in the Vienna Ab Initio Simulation Package (VASP)[6–9]. Since the initial dataset included diverse materials, we consistently applied the D3 dispersion correction[10] to account for van der Walls interactions which may be sizable in some compounds. Spin-polarization was used on-demand for compounds that might have unpaired electrons. The Hubbard U correction[11] was applied for transition metals with U values as used in the Materials Project database[1]. The plane-wave cut-off was set to 400 eV. The 2s2p oxygen electrons were treated as valence states. The supercell size was at least 6 Å in each crystallographic direction; a typical supercell consisted of about 50–120 atoms (the number of hydrogen atoms was on the order of ~10 to ~50). Brillouin Zone integration was performed in the Γ point only. The crystal structures were retrieved from the Materials Project database[1]. The AIMD simulations were run in the isothermal–isochoric (*NVT*) ensemble with the Nosé–Hoover thermostat[12,13] using fixed cell parameters, as obtained from the database. To reduce the computational time, we used deuterons (2 Da) with 1 fs time step. To speed up some of the calculations, we employed machine learning force-fields (MLFF) which were trained on-the-fly during AIMD simulations (MLFF–AIMD), as implemented in the VASP code[14–16]. The MLFF–AIMD method is robust and executes MD with nearly *ab initio* accuracy. It is particularly reliable since it resorts to *ab initio* calculation of forces whenever the MLFF needs to be retrained. Our results support the credibility of the MLFF method. Thus, the AIMD conductivity of $CsHSO_4$ (mp-1192419, Fig. 7) is 0.0083 S/cm at 650 K with a confidence interval of approximately 0.0025 S/cm to 0.0141 S/cm. The MLFF–AIMD conductivity is 0.0051 S/cm, which is well within the limits and the difference can be attributed to the natural variability of independent MD runs. The analysis of the force-field errors further confirms that MLFF–AIMD simulations are reliable. The typical root-mean-square errors of energies and forces are 0.001 eV/atom and 0.114 eV/Å, respectively ($CsHSO_4$ @650 K). These errors are relatively small for MD and are comparable to other state-of-the-art neural network fore-fields such as CHGNet (0.033 eV/atom and 0.079 eV/Å)[17]. For other compounds, e.g., $Sr(HSO_4)_2(H_2SO_4)$ and $Ba(H_2PO_4)_2$ in Fig. 7, the typical errors are comparable, on the order of 0.001 eV/atom and 0.1 eV/Å. These figures of merit, the good agreement between AIMD and

MLFF–AIMD and the small errors in energies and forces, support the credibility of our MLFF–AIMD simulations.

Few words should be said regarding the *NVT* ensemble employed in this work. Because the simulations were performed in the *NVT* ensemble, structural transitions to superprotonic phases were not directly captured. Nevertheless, even with the confines of the unit cells defined by the room temperature, non-superprotonic phases, our elevated temperature AIMD simulations achieve thermal activation of the polyanion group rotation and disordering of hydrogen bonds. Given this crystallographic constraint, we expect that the so-calculated diffusivities provide a lower bound of the true values that would be obtained with temperature-dependent lattice parameters. (At present, the computational cost of explicit modelling of superprotonic transitions in AIMD is prohibitive.)

Initial dataset: Proton diffusivities (D_H) of compounds in the initial dataset were assessed by AIMD runs using 25 ps long trajectories at 700 K. $D_H = \lim_{t\to\infty} \langle R_H^2 \rangle / 6t$, where $\langle R_H^2 \rangle$ is the mean-squared displacement of protons (R_H) and t is time. We calculated the D_H as the fit of $\langle R_H^2 \rangle$ vs. t obtained from AIMD. The calculated D_H values were used to test the proposed descriptors. To differentiate between fast and poor proton conductors in the initial dataset, we applied the cut-off for D_H that was set to 10^{-6} cm^2/s. This was necessary to filter out trajectories that did not result in any long-range diffusion. Proton excursions from the local equilibrium can produce mean-squared displacement of about 1 Å^2, resulting in an apparent D_H of about [1 Å^2 / (6×simulation time)], even in the absence of any diffusion. For 25 ps trajectory, this corresponds to about 10^{-6} cm^2/s. In other words, this cut-off allowed us to differentiate between diffusion versus noise in the AIMD trajectories, as shown in Fig. S0 below. (This cut-off corresponds to about 0.02 S/cm conductivity at 700 K, which is within the range of experimental diffusivities[18] extrapolated by us to 700 K, i.e., from about 0.003 S/cm to 0.3 S/cm.) In addition to D_H, we also computed the metrics for each of the two steps of the Grotthuss mechanism (see Local metrics of proton transfer and polyanion rotation rates subsection below), providing further credibility to the analysis of descriptors. Further, the strong correlation between the calculated D_H and local metrics of proton transfer in Fig. S1b indicates that Grotthuss diffusion is a dominant mechanism in solid acids in good agreement with previous studies[19–21]. While the possibility of vehicle diffusion (common in many liquid electrolytes[22] and contributing to proton conductivity at oxides' grain boundaries through water interlayers[23]) cannot be entirely excluded, its contribution is considered negligible for the majority of the proton-conducting compounds in both the initial and final datasets.

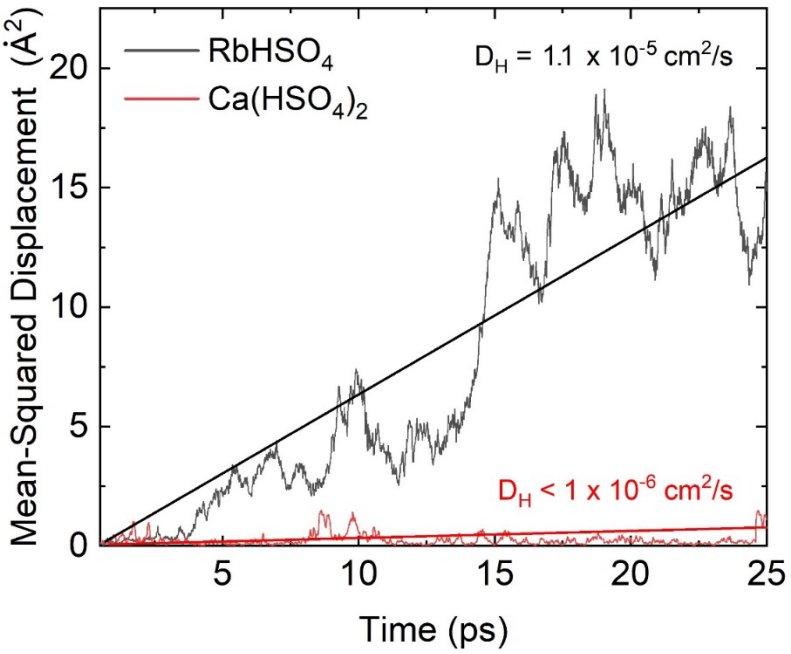

Figure S0. Mean-squared displacement of H^+ in two representative compounds: $RbHSO_4$ (fast proton diffusion) and $Ca(HSO_4)_2$ (negligible proton motion). The diffusion coefficients are calculated as a slope of the mean-squared displacement.

Final dataset (step VII): Proton diffusivities of compounds in the final dataset were assessed from the MLFF–AIMD runs at 650 K. A typical trajectory was 150 ps long. D_H was computed as outlined in *step VIII* below.

AIMD simulations at various temperatures (step VIII). For a few most promising compounds, we calculated D_H at lower temperatures (starting from 625 K and, depending on compound, down to 350 K). For each temperature, D_H was estimated from the MSD at the end of the run, $D_H \approx \langle R_{H,end}^2 \rangle / 6t_{end}$, and was averaged over multiple runs (the runs that did not show appreciable diffusivity, which was checked by the displacement of protons, were considered to have zero diffusivity for the averaging purposes). This approach was more reliable than a linear fit, especially for long runs at low-temperature showing a lower diffusivity (see example in Fig. S6). These runs employed AIMD (or MLFF–AIMD) and were up to 2 ns long. Proton conductivity, σ_H, was calculated by using the Nernst–Einstein relation: $\sigma_H = ((Ze)^2 C_H)/k_B T) D_H$, where Z is the proton charge, e is the elementary charge, $C_H = N_H/V$ is the total number of protons (N_H) per supercell volume (V), and D_H is the proton diffusion coefficient averaged over all protons in the simulation.

Phonon spectra calculations

Phonons were calculated using the finite-difference method as implemented in the VASP code [3,6–9] (without D3 correction). Supercells and atomic positions were fully relaxed, so that forces acting on atoms were below 10^{-3} eV/Å. The plane-wave cut-off energy was set to 520 eV. The phonon

band center (for each atom) was then calculated[24]. We also calculated the power spectra from the AIMD for each atomic species from the respective velocity autocorrelation functions[25].

Assignment of pK_a values to proton donor and proton acceptor groups

The pK_a of an acid group is defined with respect to the K_a, the acid dissociation constant, i.e., the equilibrium constant of the $HA = A^- + H^+$ reaction, and $K_a = [A^-][H^+]/[HA]$, $pK_a = -\log_{10} K_a$ and $\Delta G = -RT \ln K_a$. As the first step in assigning pK_a descriptors, the donor and acceptor sites, as well as corresponding donor and acceptor (polyanion) groups, associated with each proton in the crystal structure were identified by assessing the spatial connectivity of atoms and the respective bond lengths. Each donor and acceptor group was then assigned an acidity constant (pK_a) value from the literature (see Table S3; compounds with groups that have no tabulated pK_a values were excluded from consideration) [26–29]. Here we primarily use pK_a tabulated for acids in water. For the acceptor groups, we used the pK_a value of the conjugated acid (protonated group, i.e., after the proton transfer from the donor site to the acceptor site would have occurred). We then assign $\Delta pK_a = |pK_{a,donor} - pK_{a,acceptor}|$ as a descriptor that shows the difference in acidity between the proton bonded to its initial donor and the proton bonded to its initial acceptor.

Local metrics of proton transfer and polyanion rotation rates

Beyond computing macroscopic diffusivity, we assess individual metrics for each of the two steps of the Grotthuss mechanism. To assess the rate of proton transfer, we calculate the maximal distance between the proton and its initial donor atom encountered with the 25 ps simulation period, $L_{OH,max}$ (Figure 1a). This parameter, which has a value close to d_{OH} at the initiation of the simulation, reveals whether any proton transfer took place during the allocated time (Figure 1b). To assess the rate of polyanion group rotation, we calculate the standard deviations σ_θ and σ_φ of spherical angles θ (polar) and φ (azimuthal) of all bond vectors (e.g., S–O in the SO_4 group, in the internal coordinate system associated with the initial vector orientation) tracking displacement from their initial orientation over time (Figure 1c), and use the larger one of them, i.e., $max(\sigma_\theta, \sigma_\varphi)$ as descriptor. We note that although the proton transfer and rotation of polyanion groups are often correlated[19,30], our analysis shows that these two metrics (viz., $L_{OH,max}$ and maximal standard deviation of the rotation angles) are nevertheless indicative of the rates of the two rate-limiting steps (i.e., we can infer which step is rate limiting, see Figure S1). This assessment therefore allows us to correlate each descriptor with both diffusivity and the metric of respective step, making our analysis more robust (see Results and Discussions).

Section S2. Supporting Figures S1–S8

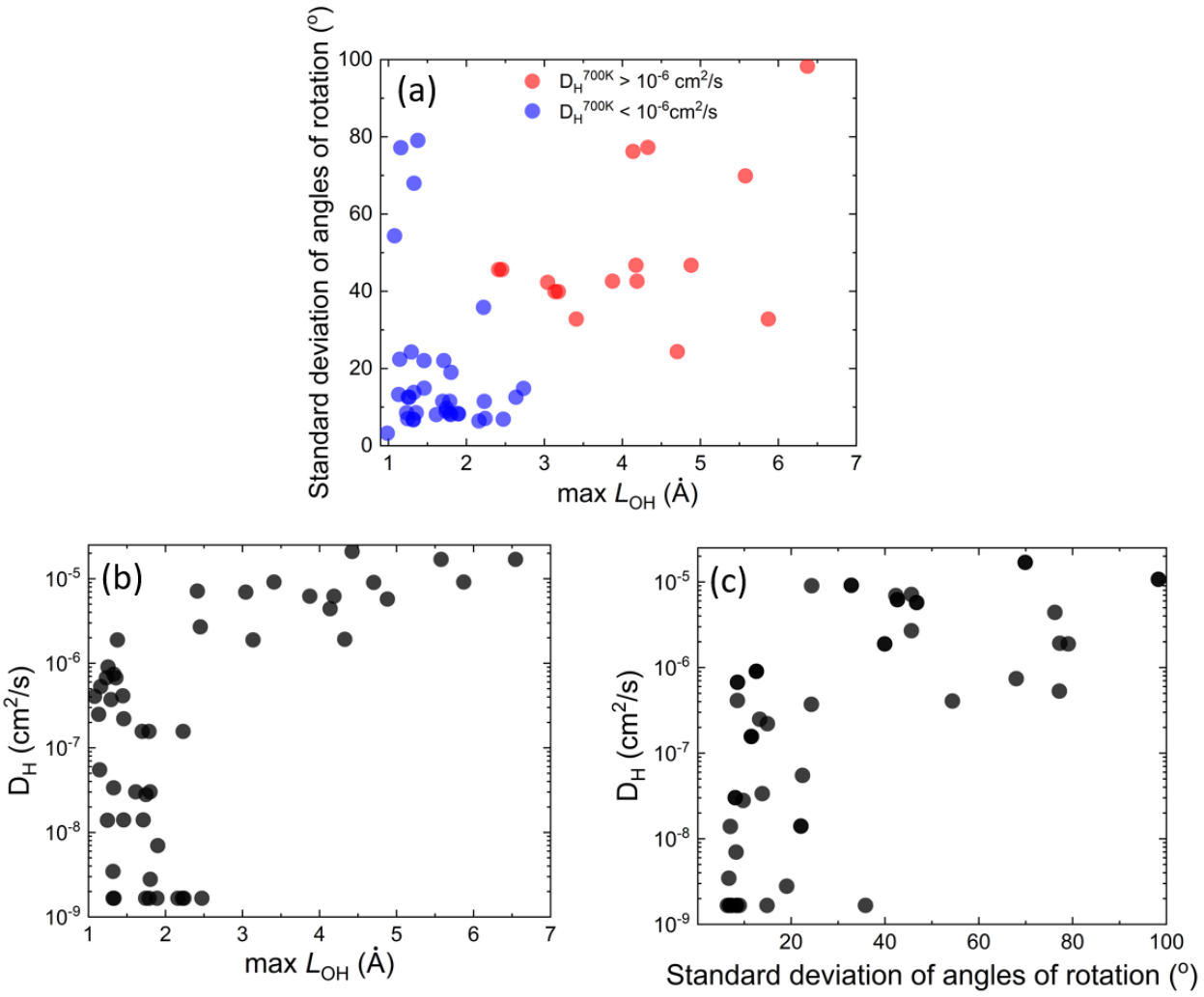

Figure S1. Analysis of limiting factors for two steps of the Grotthuss proton transport. (a) The scatter plot of rotational metric (the largest of the θ and φ standard deviations) vs. maximal distance L_{OH} between the proton and its initial donor atom showing limiting factors of proton diffusion in the preselected set of compounds for group rotations and local proton transfer, correspondingly. Materials demonstrating a long-range hydrogen diffusion are in red. (b) Scatter plot of D_H vs. *max* L_{OH}. (c) Scatter plot of D_H vs. the rotational metric.

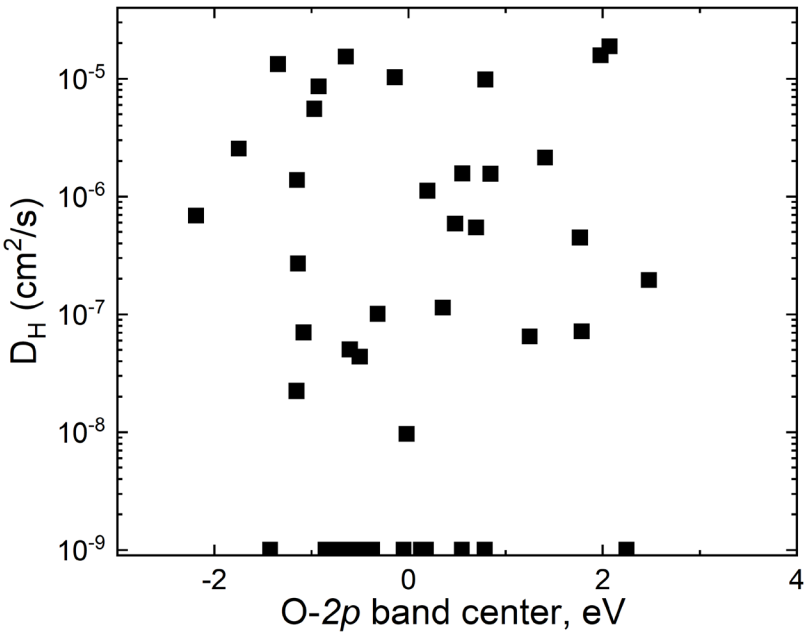

Figure S2. Scatter plot of diffusion coefficient D_H vs. O-2p band center for the subset of materials from the initial dataset. No generalizable correlation is observed.

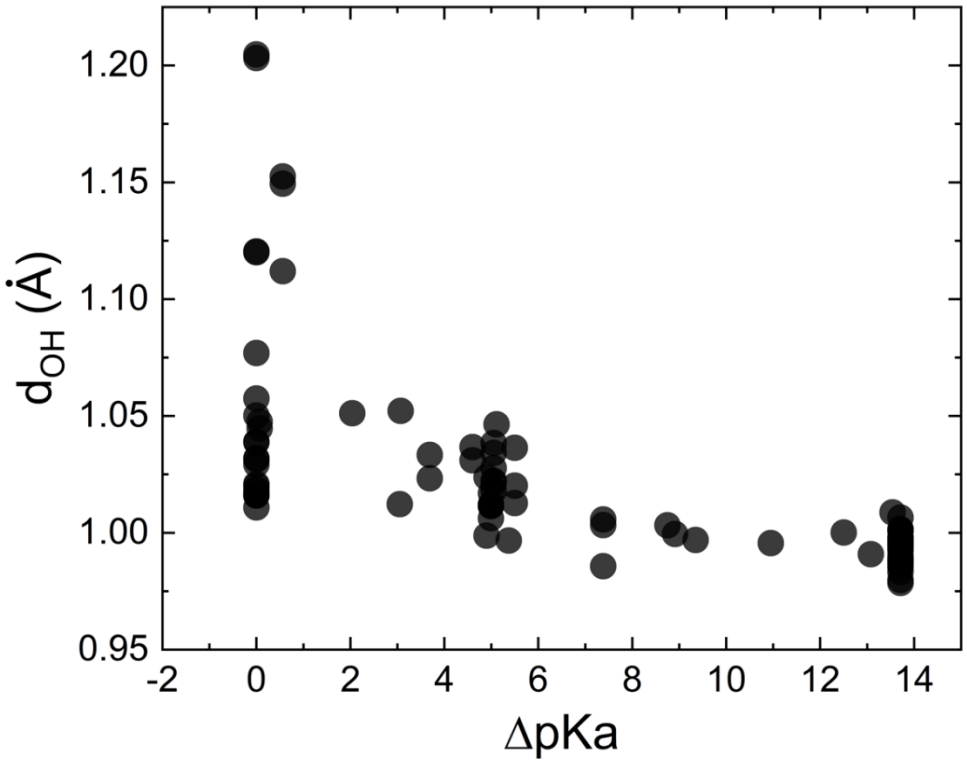

Figure S3. A scatter plot showing maximal initial O–H bond length d_{OH} vs. ΔpK_a.

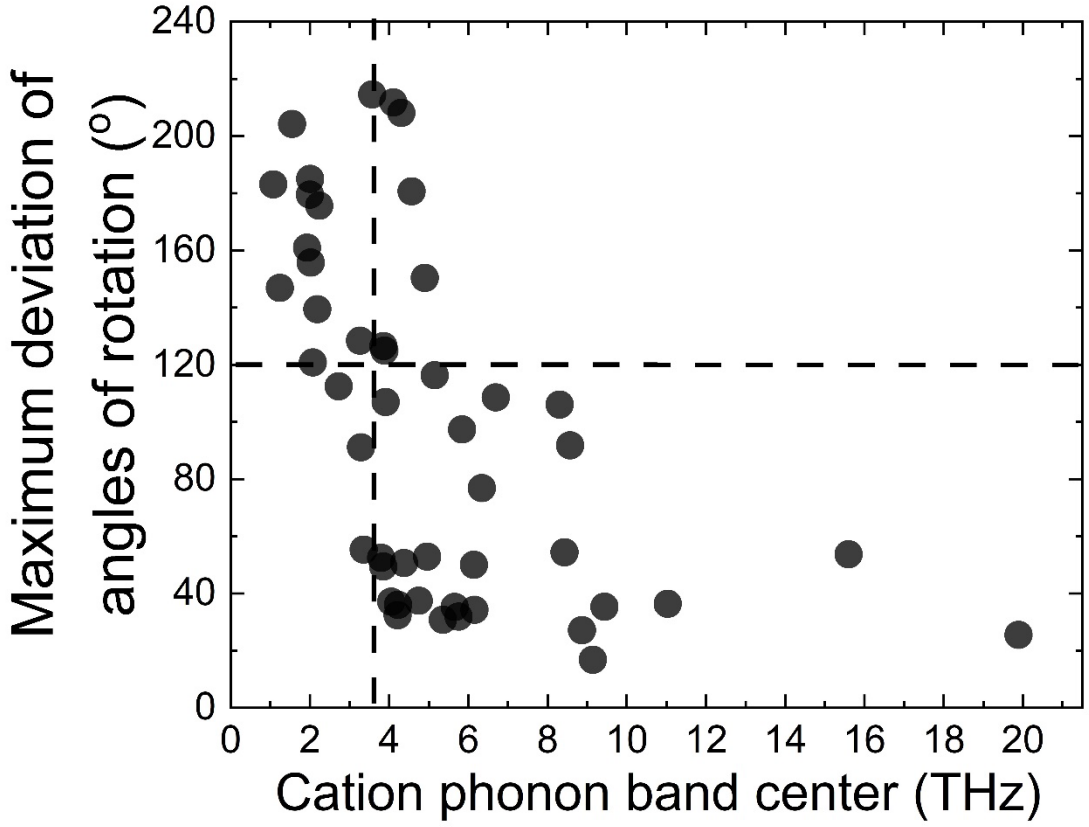

Figure S4. AIMD results from the initial dataset to extract group rotation descriptors: Complementary rotational metric (the maximal of the θ and φ angles as observed in AIMD) vs. cation phonon band center. Compounds that do not possess mono-oxyanion groups were excluded from analysis (Table S1). All data at 700 K.

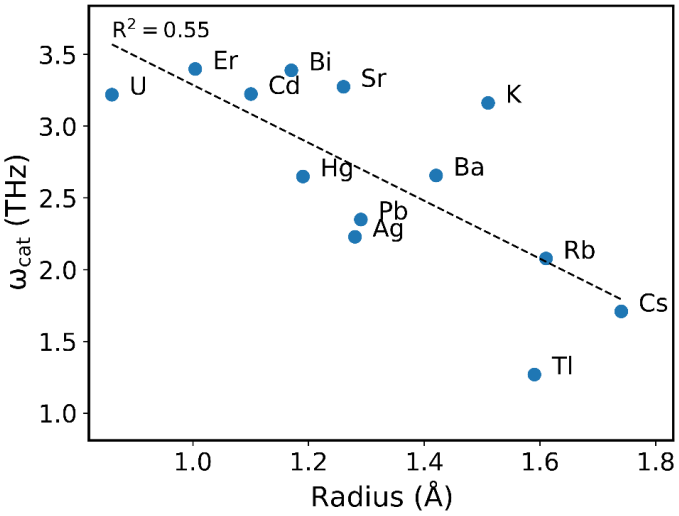

Figure S5. Average cation phonon band center vs. ionic radius[31].

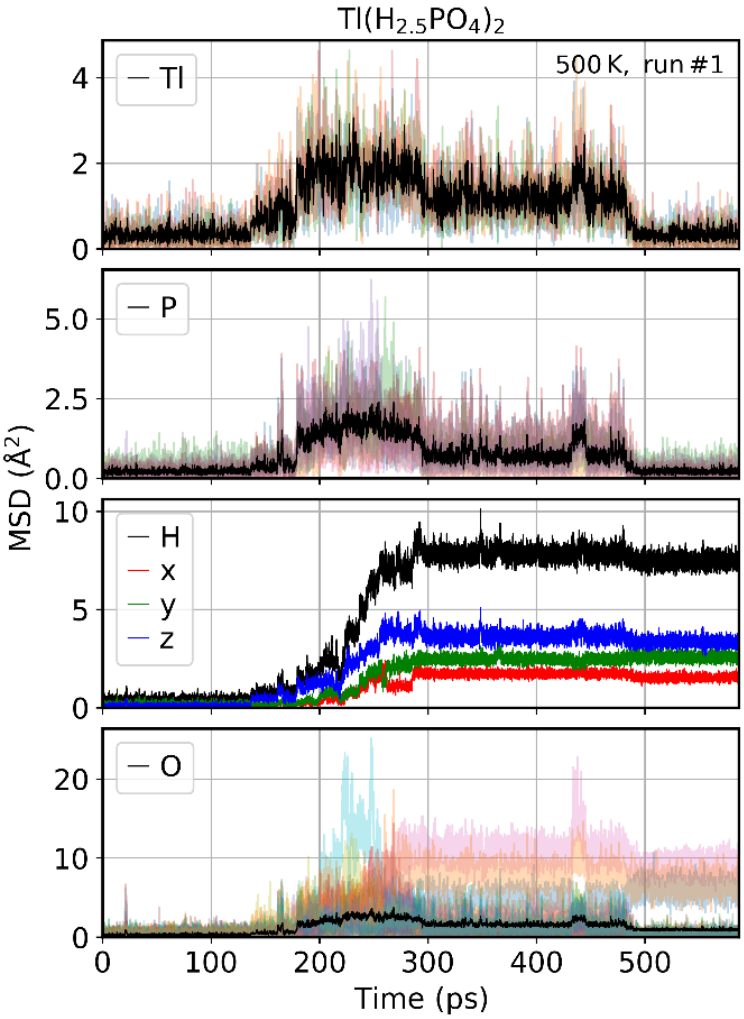

Figure S6. MSD vs. time plot for $Tl(H_{2.5}PO_4)_2$ (mp-696762) at 500 K (*NVT* simulation). Each panel show one type of atoms (Tl, P, H, O). Black lines show the average MSD (for each atom type). For Tl, P, O, also MSD of each individual atom is shown (different colors). For H, only the average MSD is shown (and x, y, z components of the MSD). In about first 150 ps no diffusion events were observed. Diffusion of hydrogen is accompanied by rotations of oxyanions (MSD of O) and displacement of Tl atoms. In fact, the whole crystal changes the structure (see radial distribution function (RDF) in Fig. S7).

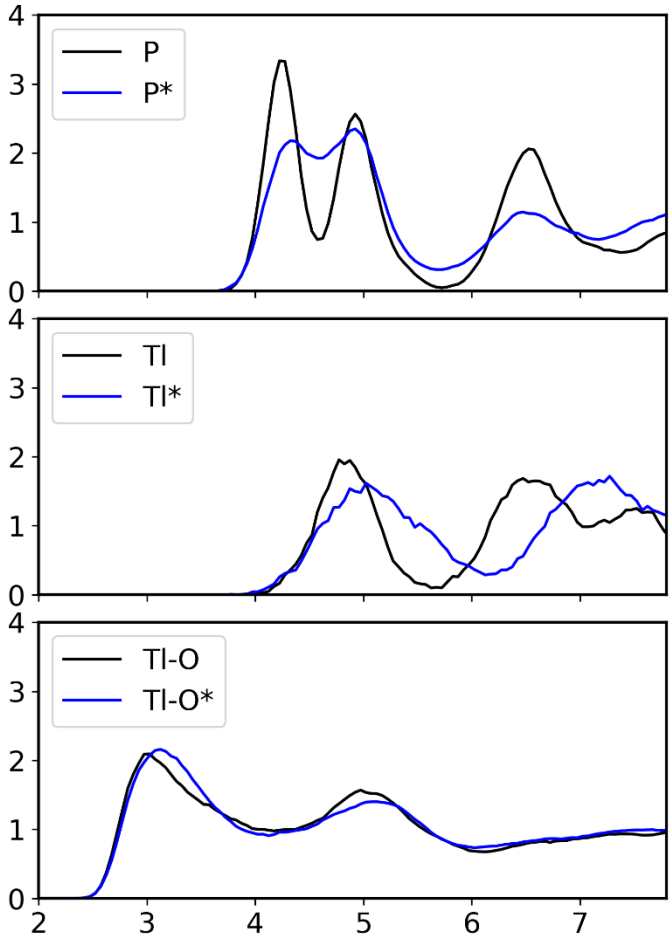

Figure S7. Radial distribution functions (RDFs) of P–P, Tl–Tl, and Tl–O ($Tl(H_{2.5}PO_4)_2$ at 500 K, *NVT* simulation). The black line corresponds to the 0 ps ≤ t < 100 ps interval, where no diffusion happened (see Fig. S6). The blue line corresponds to the 200 ps ≤ t < 300 ps interval, where proton diffuses (see Fig. S6).

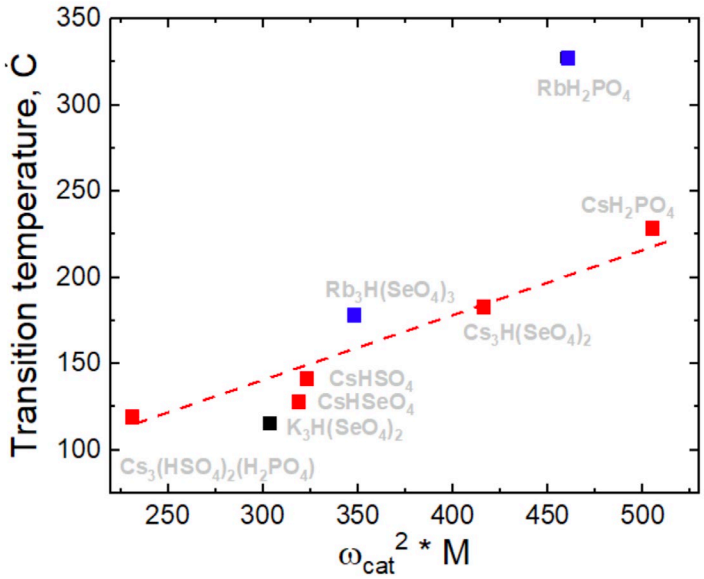

Figure S8. Experimental temperatures of superprotonic transition for Cs, Rb, K-based solid acids taken from references[32–41] vs. force constants associated with cation phonon band center. The line is the guide to the eye.

Section S3. Supporting Tables S1–S3

Table S1. List of compounds in the initial dataset. Compounds demonstrating fast proton diffusion at 700K (AIMD) are highlighted in bold; compounds that melted are marked with * (these compounds were excluded from further analysis); compounds that do not have mono-oxyanion groups (XO_n) are highlighted with † (these compounds were excluded from analysis of group rotation metrics).

MP-ID	Formula
mp-707424	$Al_2H_{12}(SeO_5)_3$ †
mp-850293	$Al_2H_{16}S_3O_{20}$ †
mp-722527	$AlH_{11}SO_{10}$ *
mp-1196038	$Ba_2B_{11}H_7O_{22}$
mp-1199009	$Ba_3B_6H_2O_{13}$ †
mp-23904	BaH_4O_3 †
mp-642844	BaH_5BrO_3 †
mp-642834	BaH_5ClO_3 †
mp-28587	BaH_8O_5 †
mp-626973	$Ba(HO)_2$ †
mp-706400	$BaP_2(HO_2)_4$
mp-720433	$Be_2As(HO)_9$ †
mp-23883	Be_2BHO_4 †
mp-24674	$Be_3P_2(H_2O_5)_2$ †
mp-757836	BeH_2SeO_4 †
mp-23996	BeH_8SO_8 *
mp-24348	BiP_4HO_{12} †
mp-1198782	$Ca_2Al_3H_3O_8$ †
mp-706291	$Ca_2B_8H_2O_{15}$ † *
mp-722262	$CaB_3H_3O_7$ †
mp-23701	$CaB_8H_4O_{15}$ †
mp-703574	$CaH_2(SO_4)_2$
mp-643898	$CaP_2H_2O_7$ †
mp-697657	$CaP_4(HO_6)_2$ †
mp-24390	$CaPHO_4$
mp-1197015	$CdP_2(H_4O_5)_2$
mp-743538	$CrH_{18}(O_3F)_3$ †
mp-758948	$Cs_2H_6CO_6$ *
mp-867975	$CsB_2H_5O_6$ †
mp-23742	$CsB_5(H_2O_3)_4$ †
mp-1192419	**$CsHSO_4$**
mp-1195974	**$CsP_2H_5O_8$**
mp-1197651	**$CsP(HO_2)_2$**
mp-1202664	$ErH_2Cl_3O_{13}$
mp-24640	**$ErH_3(SO_4)_3$**
mp-707317	ErP_4HO_{12} †
mp-643564	FeH_2SO_5
mp-24465	$GaP_3(HO_5)_2$ †
mp-697339	$Ho_2H_4CO_7$
mp-1195109	HoP_4HO_{12} †

mp-560314	$In_2H_{10}S_3O_{17}$
mp-762358	**$LaH_9(SO_6)_2$**
mp-757220	$LuH_6(ClO_5)_3$
mp-699232	$Mg_7P_2(HO_2)_8$
mp-23748	$MgBHO_3$ †
mp-24006	$MgH_{12}(BrO_6)_2$
mp-1202344	$MgH_{12}(ClO_6)_2$ *
mp-504894	$MgH_{12}SeO_9$
mp-24041	MgH_2SO_5
mp-24460	**$MgH_6(SO_4)_4$**
mp-865188	$MgH_8(ClO_6)_2$
mp-24620	$MgMoH_2O_5$
mp-24071	**$MnH_6(SO_4)_4$**
mp-865024	$MnP_2H_2O_7$ †
mp-1203000	**$NdH_{11}S_3O_{16}$**
mp-24574	**$NdH_5(SeO_4)_2$**
mp-757886	$NdHS_3O_{11}$
mp-1181715	$NiH_{10}(SeO_5)_2$
mp-1180537	$NiH_{12}(ClO_6)_2$*
mp-559054	$NiH_{12}SO_{10}$ *
mp-23877	$NiH_{14}SO_{11}$ *
mp-1202294	$NiP_2H_2O_7$ †
mp-698164	$Rb_2B_{10}H_6O_{19}$ †
mp-1197195	$Rb_2B_7H_5O_{14}$ †
mp-23781	$Rb_3H(SO_4)_2$
mp-863420	$Rb_4H_4C_3O_{10}$
mp-23700	RbH_2OF †
mp-28264	RbH_3O_2 †
mp-733612	**$RbH_3(SO_4)_2$**
mp-24022	**$RbH_3(SeO_3)_2$**
mp-1195562	$RbHS_2O_7$ †*
mp-1195896	**$RbHSO_4$**
mp-1199511	**$RbP_2H_5O_8$**
mp-23667	**$RbP(HO_2)_2$**
mp-24128	ReH_4NO_4 *
mp-541015	$ScH_{13}Cl_2O_7$ †*
mp-756748	$ScH_3(ClO_5)_2$
mp-696457	$ScP_3(HO_2)_6$
mp-542237	SmP_4HO_{12} †
mp-1201690	$Sr_3B_6H_2O_{13}$ †
mp-1195189	TbP_4HO_{12} †
mp-696762	**$TlP_2H_5O_8$**
mp-24656	$YH_3(SO_4)_3$
mp-24335	$YH_5(SeO_4)_2$
mp-24502	$ZnH_2(SO_4)_2$
mp-643066	ZnH_2SO_5
mp-706386	$ZrH_6O_3F_4$ †
mp-1192835	$ZrH_6(OF_3)_2$ †

Table S2. List of 143 compounds that passed the screening criteria (plus one extra compound, see †). d_{OH} is the maximal O–H distance in the pristine compound (such that either O donor atom or O acceptor atom, or both, belong to the mono-oxyanion group). ω_{cat} is the cation phonon band center (for compounds with multiple cations, the lowest value is provided). D_H is the hydrogen diffusivity as calculated at 650 K (MLFF—AIMD). The second to last column marks compounds that melted during MD ("melted", i.e., MSD of any cation exceeded 10 Å^2). The part of trajectory where compound melted was discarded and not used for D_H calculation. The last column provides comments and * marks promising compounds that showed fast diffusion and/or diffusional event(s) in MD.

#	MP-ID	Formula	d_{OH} (Å)	ω_{cat} (THz)	D_H (cm^2/s)	Melting	Comments
1	mp-867593	$Ag_2H_4(SO_4)_3$	1.031	2.22	–	melted	*; fast diffusion prior to melting
2	mp-24072	$AgH_5S_2O_9$	1.037	2.15	1.26E-05	melted	*
3	mp-707734	$AsHPb_4(ClO)_4$	1.013	2.06	1.60E-08		
4	mp-504751	$AsHPbO_4$	1.214	2.39	1.51E-08		
5	mp-758007	$Ba_2CaP_4(H_3O_8)_2$	1.036	2.66	1.64E-08		
6	mp-1199629	$Ba_2CdP_4(H_3O_8)_2$	1.028	2.69	1.84E-08		
7	mp-735530	$Ba_2Fe_3P_6HO_{22}$	1.200	2.59	1.03E-08		
8	mp-1194837	$Ba_3As_2H_{34}O_{25}$	1.015	2.78	1.33E-06	melted	*
9	mp-23806	$BaAsH_3O_5$	1.015	2.59	2.03E-08		
10	mp-23810	$BaAsHO_4$	1.045	2.63	1.55E-08		
11	mp-733968	$BaCaP_2(HO_4)_2$	1.058	2.53	1.28E-08		
12	mp-698325	$BaH_4(CO_2)_3$	1.113	2.68	5.71E-08		
13	mp-1199471	$BaNaAlMo_6(H_{13}O_{17})_2$	1.018	2.37	1.22E-05	melted	
14	mp-706400	$BaP_2(HO_2)_4$	1.023	2.69	1.52E-08		
15	mp-706543	$BaP_2(HO_2)_4$	1.210	3.14	1.13E-05	melted	*

16	mp-698163	$BaPHO_4$	1.050	2.53	3.46E-08		
17	mp-1105235	$BH(PbO_2)_2$	1.016	2.60	1.82E-08		
18	mp-1200655	$BiH_{25}C_8(SO_2)_6$	1.012	3.39	9.25E-06		*
19	mp-1202482	$Cd_3H_{18}S_4N_2O_{21}$	1.012	3.19	2.39E-07		
20	mp-1197015	$CdP_2(H_4O_5)_2$	1.022	3.26	5.26E-08		
21	mp-733936	$Cs_2MgH_8(CO_5)_2$	1.016	1.86	2.90E-07		*
22	mp-1181702	$Cs_3H(SeO_4)_2$	1.056	1.66	1.16E-06		*
23	mp-1192732	$Cs_3H(SeO_4)_2$	1.224	1.63	5.93E-07		*
24	mp-23980	$Cs_3H(SeO_4)_2$	1.227	1.70	2.91E-08		*
25	mp-1197340	$Cs_4AsH_5Se_3O_{16}$	1.056	1.54	2.55E-07		
26	mp-1185571	$CsAs(HO_2)_2$	1.056	1.82	3.06E-08		
27	mp-24141	$CsHSeO_4$	1.031	1.52	3.07E-06		*
28	mp-1192419	$CsHSO_4$	1.030	1.82	4.71E-06		*
29	mp-540981	CsHSO4	1.023	1.69	1.53E-05	melted	*
30	mp-557752	$CsHSO_4$	1.212	1.52	3.97E-08		*
31	mp-1195974	$CsP_2H_5O_8$	1.121	1.24	3.33E-07		*
32	mp-1198944	$CsP_2H_5O_8$	1.203	1.41	2.38E-08		
33	mp-1191996	$CsP_2(HO_2)_3$	1.145	1.30	2.30E-08		
34	mp-574928	$CsPH_3O_3F$	1.039	1.67	2.90E-07		*
35	mp-542541	$CsPH_3O_4F$	1.032	2.65	7.32E-07		*

36	mp-1188121	$CsP(HO_2)_2$	1.061	1.96	2.30E-08		
37	mp-1197651	$CsP(HO_2)_2$	1.048	2.05	2.54E-08		
38	mp-542557	$CsScAs_2(HO_4)_2$	1.015	1.72	3.21E-08		
39	mp-24640	$ErH_3(SO_4)_3$	1.008	3.40	1.62E-06		*
40	mp-757360	$HgTe(HO)_7$	1.013	2.65	1.86E-07		*
41	mp-24350	$K_2CoH_8(CO_5)_2$	1.0214	3.28	1.51E-08		
42	mp-604071	$K_2FePH_5(CO_5)2$	1.0207	3.12	7.97E-08		
43	mp-733853	$K_2HI_2ClO_6$	1.0242	3.2	2.58E-08		
44	mp-757963	$K_2MgH_8(CO_5)_2$	1.024	3.28	4.95E-08		
45	mp-850535	$K_2Mn_3H_{10}S_4O_{21}$	1.0147	2.95	3.47E-07		
46	mp-695963	$K_2NaH_{10}IO_{10}$	1.0163	3.29	1.42E-07	melted	
47	mp-505771	$K_2NaH_5(CO_4)_2$	1.0835	3.21	1.30E-07		
48	mp-766427	$K_2NaZn_2H_5(C_2O_7)_2$	1.2168	3.15	1.52E-08		
49	mp-24573	$K_2NiH_8(CO_5)_2$	1.0225	3.36	1.49E-08		
50	mp-721562	$K_2P_3H_5O_{11}$	1.1	3.02	3.18E-08	melted	
51	mp-707096	$K_2P_3H_7O_9$	1.0478	3.23	1.10E-07		*
52	mp-723043	$K_2TeH_6SeO_{10}$	1.0115	2.85	2.42E-07		
53	mp-867184	$K_2TeH_6SeO_{10}$	1.0139	2.9	4.77E-07		
54	mp-697127	$K_3HPdS_2(ClO_3)_2$	1.2044	3.15	2.63E-08		
55	mp-706983	$K_3HPtS_2(ClO_3)_2$	1.2023	3.19	2.28E-08		

56	mp-1200107	$K_3HS_3O_{11}$	1.016	3.1	4.50E-08		
57	mp-23979	$K_3H(SeO_4)_2$	1.2241	3.08	5.29E-06		*
58	mp-23779	$K_3H(SO_4)_2$	1.2177	3.31	4.88E-07		*
59	mp-557941	$K_4AsH_5S_3O_{16}$	1.0373	3.19	3.66E-07		*
60	mp-746688	$K_4MnH_6(S_2O_9)_2$	1.0316	3.29	1.20E-07		
61	mp-697128	$KCa_2P_4H_{11}O_{18}$	1.1958	3.23	8.48E-08		
62	mp-746371	$KCo_2As_2HO_8$	1.0755	3.13	1.80E-08		
63	mp-735586	$KFe_2H(SeO_3)_4$	1.0289	3.19	1.97E-08		
64	mp-23682	$KH_3(CO_2)_2$	1.1421	3.1	2.43E-06	melted	
65	mp-1198088	KH_3CO_6	1.0096	3.02	2.35E-07		
66	mp-1180593	$KH_3(SeO_3)_2$	1.047	3.38	2.29E-07		*
67	mp-706579	$KH_3(SeO_3)_2$	1.2224	3.36	1.31E-07		*
68	mp-1200593	$KH_3(SeO_4)_2$	1.0748	2.6	1.43E-05	melted	*
69	mp-733655	$KH_3(SO_4)_2$	1.0466	3	5.37E-06	melted	*
70	mp-697284	KH_3SO_6	1.0198	3.28	7.59E-07		
71	mp-23724	$KHCO_3$	1.0345	3.11	3.38E-08		
72	mp-634431	$KHCO_3$	1.0368	3.49	2.80E-08		
73	mp-706273	$KH(IO_3)_2$	1.0646	3.41	2.15E-08		
74	mp-720407	$KH(IO_3)_2$	1.011	3.46	1.13E-06	melted	
75	mp-766021	$KH(IO_3)_2$	1.2187	3.42	1.93E-08		

76	mp-24433	$KHSeO_3$	1.0136	3.03	4.48E-08		
77	mp-707536	$KHSeO_4$	1.0376	3.45	1.84E-07		*
78	mp-23800	$KHSO_4$	1.0336	3.19	6.02E-08		*
79	mp-1200428	$KMgAs(H_6O_5)_2$	1.0134	2.89	4.43E-08		
80	mp-23905	$KMgH_9(CO_5)_2$	1.2182	2.76	9.98E-08		
81	mp-721617	$KMgP(H_6O_5)_2$	1.0107	2.58	4.54E-08		
82	mp-1192905	$KNaTe(HO)_6$	1.0076	3.07	1.60E-07	melted	
83	mp-697458	$KNiH_9(CO_5)_2$	1.2168	2.92	4.88E-08		
84	mp-1197171	$KP_2H_5O_8$	1.1654	2.96	2.48E-08	melted	
85	mp-706608	KPH_3O_3F	1.0287	3.49	2.55E-08		
86	mp-1197097	KPH_3O_4	1.0468	3.15	1.34E-07		*
87	mp-24214	KPH_3O_4F	1.0303	2.91	3.51E-08		
88	mp-761185	KPH_3O_4F	1.0339	3.11	2.67E-08	melted	
89	mp-1106168	$KP(HO_2)_2$	1.2088	3.37	1.58E-08		
90	mp-1198928	$KP(HO_2)_2$	1.0783	3.03	7.56E-07		*
91	mp-23959	$KP(HO_2)_2$	1.057	3.22	2.04E-08		
92	mp-24262	$KP(HO_2)_2$	1.2116	3.31	2.04E-08		
93	mp-24263	$KP(HO_2)_2$	1.2128	3.41	1.96E-08		
94	mp-696752	$KP(HO_2)_2$	1.2093	3.23	1.28E-08		
95	mp-699437	$KP(HO_2)_2$	1.0326	3.2	6.85E-06	melted	*

96	mp-757909	$KP(HO_2)_2$	1.0801	3.17	2.92E-08		
97	mp-644015	$KVHSe_2O_7$	1.2162	3.41	1.65E-08		
98	mp-541071	$KZrP_2HO_8$	1.0773	3.28	2.16E-08		
99	mp-556009	$MgTlAs(H_6O_5)_2$	1.013	1.09	5.82E-08		
100	mp-554894	$MgTlP(H_6O_5)_2$	1.011	0.88	3.16E-08		
101	mp-24731	$Ni_3AgP_3(HO_6)_2$	1.084	2.32	1.48E-08		
102	mp-24624	$Rb_2CoH_8(CO_5)_2$	1.022	2.21	1.23E-07		
103	mp-24606	$Rb_2MgH_8(CO_5)_2$	1.018	2.28	2.07E-08		
104	mp-505772	$Rb_2NaH_5(CO_4)_2$	1.0947	2.12	6.43E-06	melted	
105	mp-753854	$Rb_2PH_3SeO_8$	1.073	2.08	4.42E-07		*
106	mp-603414	$Rb_2TeH_6SeO_{10}$	1.032	1.75	8.51E-07		
107	mp-23897	$Rb_3H(SeO_4)_2$	1.224	2.26	1.12E-06		*
108	mp-1197110	$Rb_3H(SO_4)_2$	1.013	2.14	1.26E-06		*
109	mp-23781	$Rb_3H(SO_4)_2$	1.219	2.30	1.06E-06		*
110	mp-863420	$Rb_4H_4C_3O_{10}$	1.050	2.20	4.69E-08		
111	mp-707406	$Rb_6Te_3P_6(H_{13}O_{20})_2$	1.020	1.96	9.91E-08	melted	
112	mp-699453	$RbAs_2H_5O_8$	1.209	1.88	9.86E-07		*
113	mp-1196732	$RbH_2(IO_3)_3$	1.024	2.00	4.25E-07		*
114	mp-23688	$RbH_3(CO_2)_2$	1.146	2.04	–	melted	
115	mp-24022	$RbH_3(SeO_3)_2$	1.057	1.86	1.09E-07		*

116	mp-733612	$RbH_3(SO_4)_2$	1.059	1.93	6.62E-06	melted	*
117	mp-695829	$RbHSeO_4$	1.047	2.44	6.30E-08		*
118	mp-696794	$RbHSeO_4$	1.034	2.05	4.30E-07		*
119	mp-1195896	$RbHSO_4$	1.019	2.20	3.35E-06	melted	
120	mp-1197989	$RbHSO_4$	1.022	2.24	1.31E-06	melted	*
121	mp-707377	$RbHSO_4$	1.013	2.00	–	melted	
122	mp-559463	$RbMgAs(H_6O_5)_2$	1.012	1.73	3.11E-08		
123	mp-604725	$RbMgP(H_6O_5)_2$	1.014	1.86	3.06E-08		
124	mp-1199511	$RbP_2H_5O_8$	1.205	1.97	2.05E-08		
125	mp-1190228	$RbP_2(HO_2)_3$	1.127	1.68	4.12E-08		
126	mp-761252	$RbPH_3O_4F$	1.032	2.24	2.03E-08		
127	mp-703312	$RbPH_4O_5$	1.015	2.02	1.58E-06		*
128	mp-23667	$RbP(HO_2)_2$	1.053	2.17	2.20E-08		
129	mp-642831	$RbP(HO_2)_2$	1.209	2.15	1.47E-08		
130	mp-643791	$RbP(HO_2)_2$	1.210	2.29	2.19E-08		
131	mp-703528	$RbP(HO_2)_2$	1.216	2.15	2.10E-08		
132	mp-722348	$RbP(HO_2)_2$	1.029	1.81	1.76E-06	melted	*
133	mp-867132	$RbZnH_2Se_2BrO_6$	1.023	2.35	2.12E-08		
134	mp-867129	$RbZnH_2Se_2ClO_6$	1.015	2.21	1.16E-07	melted	
135	mp-510709	$SrAsH_3O_5$	1.015	3.13	2.20E-08		

136	mp-757723	$SrH_4(SO_4)_3$	1.038	3.55	2.52E-06		* †
137	mp-863961	$SrNi_2P_2(H_2O_5)_2$	1.055	3.42	1.11E-07		*
138	mp-696762	$TlP_2H_5O_8$	1.203	1.19	9.40E-07		*
139	mp-1196113	$TlP(HO_2)_2$	1.048	1.34	4.87E-08		
140	mp-643701	$TlP(HO_2)_2$	1.212	1.34	2.11E-08		
141	mp-690711	$TlP(HO_2)_2$	1.204	1.76	2.75E-08		*
142	mp-697267	$TlP(HO_2)_2$	1.051	1.30	3.26E-08		
143	mp-768283	$UAs_2H_6O_{11}$	1.016	3.22	6.61E-08		
144	mp-542045	$UTlH(SeO_4)_2$	1.009	1.25	6.03E-08		

† this compound has ω_{cat} = 3.55 THz just above the cut-off, therefore we run MLFF–AIMD to explore the potential diffusivity of this Sr-based compounds

Table S3. List of pK_a values used to calculate descriptors[26–29].

Acid	pK_a
HF	3.1
NH_4	9.24
H_2O	14
H_3O	-1.74
$HAsO_4$	11.3
H_2AsO_4	7.10
H_3PO_4	2.16
H_2PO_4	7.21
HPO_4	12.32
H_2SO_4	-3
HSO_4	2
H_2SeO_3	2.62
$HSeO_3$	8.32
HCO_3	10.3
H_2CO_3	6.3
H_3BO_3	9.2

References

1 Jain A, Ong SP, Hautier G, Chen W, Richards WD, Dacek S *et al.* Commentary: The Materials Project: A materials genome approach to accelerating materials innovation. *APL Mater* 2013; **1**: 011002.

2 Blöchl PE. Projector augmented-wave method. *Phys Rev B* 1994; **50**: 17953.

3 Joubert D. From ultrasoft pseudopotentials to the projector augmented-wave method. *Phys Rev B Condens Matter Mater Phys* 1999; **59**: 1758–1775.

4 Perdew JP, Burke K, Ernzerhof M. Generalized gradient approximation made simple. *Phys Rev Lett* 1996; **77**: 3865–3868.

5 Perdew JP, Burke K, Ernzerhof M. Erratum: Generalized gradient approximation made simple (Physical Review Letters (1996) 77 (3865)). *Phys Rev Lett* 1997; **78**: 1396.

6 Kresse G, Hafner J. Ab initio molecular dynamics for liquid metals. *Phys Rev B* 1993; **47**: 558–561.

7 Kresse G, Hafner J. Ab initio molecular-dynamics simulation of the liquid-metalamorphous- semiconductor transition in germanium. *Phys Rev B* 1994; **49**: 14251–14269.

8 Kresse G, Furthmüller J. Efficient iterative schemes for ab initio total-energy calculations using a plane-wave basis set. *Phys Rev B Condens Matter Mater Phys* 1996; **54**: 11169–11186.

9 Kresse G, Furthmüller J. Efficiency of ab-initio total energy calculations for metals and semiconductors using a plane-wave basis set. *Comput Mater Sci* 1996; **6**: 15–50.

10 Grimme S, Antony J, Ehrlich S, Krieg H. A consistent and accurate ab initio parametrization of density functional dispersion correction (DFT-D) for the 94 elements H-Pu. *J Chem Phys* 2010; **132**: 154104.

11 Dudarev SL, Botton GA, Savrasov SY, Humphreys CJ, Sutton AP. Electron-energy-loss spectra and the structural stability of nickel oxide: An LSDA+U study. *Phys Rev B* 1998; **57**: 1505.

12 Nosé S. A unified formulation of the constant temperature molecular dynamics methods. *J Chem Phys* 1998; **81**: 511.

13 Hoover WG. Canonical dynamics: Equilibrium phase-space distributions. *Phys Rev A (Coll Park)* 1985; **31**: 1695.

14 Jinnouchi R, Lahnsteiner J, Karsai F, Kresse G, Bokdam M. Phase Transitions of Hybrid Perovskites Simulated by Machine-Learning Force Fields Trained on the Fly with Bayesian Inference. *Phys Rev Lett* 2019; **122**: 225701.

15 Jinnouchi R, Karsai F, Kresse G. On-the-fly machine learning force field generation: Application to melting points. *Phys Rev B* 2019; **100**: 14105.

16 Jinnouchi R, Karsai F, Verdi C, Asahi R, Kresse G. Descriptors representing two- and three-body atomic distributions and their effects on the accuracy of machine-learned inter-atomic potentials. *J Chem Phys* 2020; **152**: 234102.

17 Deng B, Zhong P, Jun KJ, Riebesell J, Han K, Bartel CJ *et al.* CHGNet as a pretrained universal neural network potential for charge-informed atomistic modelling. *Nat Mach Intell* 2023; **5**. doi:10.1038/s42256-023-00716-3.

18 Haile SM, Boysen DA, Chisholm CRI, Merie RB. Solid acids as fuel cell electrolytes. *Nature* 2001; **410**: 910–913.

19 Kreuer K-D. Proton Conductivity: Materials and Applications. *Chemistry of Materials* 1996; **8**: 610–641.
20 Kreuer KD. Fast proton conductivity: A phenomenon between the solid and the liquid state? *Solid State Ion* 1997; **94**: 55–62.
21 Baranov AI. Crystals with disordered hydrogen-bond networks and superprotonic conductivity. Review. *Crystallography Reports* 2003; **48**: 1012–1037.
22 Fischer SA, Dunlap BI, Gunlycke D. Correlated dynamics in aqueous proton diffusion. *Chem Sci* 2018; **9**. doi:10.1039/c8sc01253a.
23 Miyoshi S, Akao Y, Kuwata N, Kawamura J, Oyama Y, Yagi T *et al.* Low-temperature protonic conduction based on surface protonics: An example of nanostructured yttria-doped zirconia. *Chemistry of Materials* 2014; **26**. doi:10.1021/cm5012923.
24 Muy S, Bachman JC, Giordano L, Chang HH, Abernathy DL, Bansal D *et al.* Tuning mobility and stability of lithium ion conductors based on lattice dynamics. *Energy Environ Sci* 2018; **11**: 850–859.
25 Smith JG, Siegel DJ. Low-temperature paddlewheel effect in glassy solid electrolytes. *Nature Communications 2020 11:1* 2020; **11**: 1–11.
26 Evans DA, Ripin DH. pKa's of Inorganic and Oxo-Acids. https://www.wanglab.chem.pitt.edu/wp-content/uploads/2017/09/Evans-D.-A.-Ripin-D.-H.-The-Evans-pKa-Table-Harvard-2006.pdf (accessed 12 Feb2024).
27 Peacock CJ, Nickless G. The Dissociation Constants of some Phosphorus(V) Acids. *Zeitschrift fur Naturforschung - Section A Journal of Physical Sciences* 1969; **24**: 245–247.
28 Engineering ToolBox, (2017). Inorganic Acids and Bases - pKa Values. https://www.engineeringtoolbox.com/pKa-inorganic-acid-base-hydrated-metal-ion-monoprotic-diprotic-triprotic-tetraprotic-d_1950.html (accessed 12 Feb2024).
29 Haynes WM (ed.). *CRC Handbook of Chemistry and Physics*. 95th Edition. Taylor & Francis, 2014.
30 Dreßler C, Sebastiani D. Effect of anion reorientation on proton mobility in the solid acids family CsH: YXO4 (X = S, P, Se, y = 1, 2) from ab initio molecular dynamics simulations. *Physical Chemistry Chemical Physics* 2020; **22**: 10738–10752.
31 Database of Ionic Radii, http://abulafia.mt.ic.ac.uk/shannon/ptable.php. .
32 Jiráak Z, Dlouhá M, Vratislav S, Balagurov AM, Beskrovnyi AI, Gordelii VI *et al.* A neutron diffraction study of the superionic phase in CsHSO4. *Physica Status Solidi (a)* 1987; **100**: K117–K122.
33 Haile SM, Lentz G, Kreuer KD, Maier J. Superprotonic conductivity in Cs3(HSO4)2(H2PO4). *Solid State Ion* 1995; **77**: 128–134.
34 Zakharov MA, Troyanov SI, Kemnitz E. Superprotonic high temperature phase and refinement of the low temperature structure of cshseo4. *Zeitschrift fur Kristallographie* 2001; **216**: 172–175.
35 Boysen DA, Haile SM, Liu H, Secco RA. High-temperature behavior of CsH2PO4 under both ambient and high pressure conditions. *Chemistry of Materials* 2003; **15**: 727–736.
36 Lavrova G V., Burgina EB, Matvienko AA, Ponomareva VG. Bulk and surface properties of ionic salt CsH5(PO4)2. *Solid State Ion* 2006; **177**: 1117–1122.
37 Ikeda A, Haile SM. The thermodynamics and kinetics of the dehydration of CsH2PO4 studied in the presence of SiO2. *Solid State Ion* 2012; **213**: 63–71.

38 Sanghvi S, Haile SM. Crystal structure, conductivity, and phase stability of Cs3(H1.5PO4)2 under controlled humidity. *Solid State Ion* 2020; **349**: 115291.
39 Yi D, Sanghvi S, Kowalski CP, Haile SM. Phase Behavior and Superionic Transport Characteristics of (MxRb1- x)3H(SeO4)2 (M = K or Cs) Solid Solutions. *Chemistry of Materials* 2019; **31**: 9807–9818.
40 Chisholm CRI, Haile SM. Superprotonic behavior of Cs2(HSO4)(H2PO4) - a new solid acid in the CsHSO4-CsH2PO4 system. *Solid State Ion* 2000; **136–137**: 229–241.
41 Chisholm CRI, Merle RB, Boysen DA, Haile SM. Superprotonic phase transition in CsH(PO3H). *Chemistry of Materials* 2002; **14**: 3889–3893.